PROSTHETICS

Preclinical upper limb neurorobotic platform to assess, rehabilitate, and develop therapies

Maria Pasquini[1,2]†, Nicholas D. James[3,4,5]†, Inssia Dewany[3,4,5]†, Florent-Valéry Coen[6], Newton Cho[3,4,5], Stefano Lai[1], Selin Anil[3,4,5], Jacopo Carpaneto[1], Quentin Barraud[3,4,5], Stéphanie P. Lacour[6], Silvestro Micera[1,2]*‡, Grégoire Courtine[3,4,5]*‡

Numerous neurorehabilitative, neuroprosthetic, and repair interventions aim to address the consequences of upper limb impairments after neurological disorders. Although these therapies target widely different mechanisms, they share the common need for a preclinical platform that supports the development, assessment, and understanding of the therapy. Here, we introduce a neurorobotic platform for rats that meets these requirements. A four-degree-of-freedom end effector is interfaced with the rat's wrist, enabling unassisted to fully assisted execution of natural reaching and retrieval movements covering the entire body workspace. Multimodal recording capabilities permit precise quantification of upper limb movement recovery after spinal cord injury (SCI), which allowed us to uncover adaptations in corticospinal tract neuron dynamics underlying this recovery. Personalized movement assistance supported early neurorehabilitation that improved recovery after SCI. Last, the platform provided a well-controlled and practical environment to develop an implantable spinal cord neuroprosthesis that improved upper limb function after SCI.

INTRODUCTION

Numerous neurological disorders irreversibly impair upper limb motor functions. Individuals suffering from such impairments place a high priority on the recovery of upper limb functions (*1*, *2*). This unmet clinical need has triggered the development of numerous therapies ranging from neurorehabilitation programs to neuroprosthetic and biological repair interventions (*3*). Although these therapies target diverse mechanisms, they share the dependence on a preclinical experimental environment wherein the therapy can be developed, evaluated, and understood with high-precision tools and well-controlled conditions.

Neurorobotic platforms combine numerous advantages to establish such preclinical experimental environments (*4*–*6*). Robotic interfaces afford standardized and highly reproducible conditions that specify the type of performed movements. The attachment of the limbs or body to the robotic interface provides a practical platform wherein behaviors are contained and can be manipulated. Robotic interfaces also enable precise control over the relative level of assistance for individual components of movement. In turn, instrumentation of neurorobotic platforms with multifaceted recording modalities permits high-resolution quantification of motor performances while monitoring the neural processes that determine them (*5*). Last, robotic interfaces provide the opportunity to create artificial conditions that can be instrumental to developing therapies in preclinical models with relevance to human applications (*7*–*9*).

These advantages prompted the design of numerous robotic platforms for upper limb motor functions in rodents (*10*, *11*). For example, we previously developed a robotic system (*12*, *13*) for quantitative assessment and training of forelimb movements in mice that allowed us to study the mechanisms of recovery from stroke (*14*, *15*) and to propose new rehabilitative approaches for stroke recovery (*16*). The vast library of genetic and molecular tools available in mice provides many key advantages to dissect the neural mechanisms underlying motor control and recovery from neurological disorders (*17*). Because of their small size and limited cognitive capabilities, however, mice are not an optimal preclinical model to develop new treatments, especially those involving implanted systems. For this purpose, rat models provide more practical experimental conditions. This understanding encouraged the development of several systems that interface upper limb movements with robotic manipulandum in rats (*18*, *19*). Each of these robotic systems presents features that are advantageous to study motor control and develop neurorehabilitation protocols. However, they have not been conceived with the specific goal of establishing an environment that facilitates the development of new therapies, leveraging all the unique advantages of neurorobotic platforms for this purpose. For example, most of these systems were restricted to one degree of freedom (DOF) (*20*, *21*), whereas natural reaching and grasping involves movements within the entire body workspace. Moreover, they also did not take advantage of robotic environments to enable unconstrained multifaceted recording capabilities, which are critical to develop and assess therapies. Last, they did not seek to create experimental conditions that may be unnatural for rats but could be instrumental to study and enable motor control after injury (*22*). Here, we aimed to incorporate these advantages into the conception of a neurorobotic platform that leverages our previous mouse robotic system to support the conception, assessment, and understanding of therapies for restoring upper limb functions in rat models of neurological disorders.

[1]Biorobotics Institute and Department of Excellence in Robotics and AI, Scuola Superiore Sant'anna, Pisa, Italy. [2]Bertarelli Foundation Chair in Translational Neuroengineering, Center for Neuroprosthetics and Institute of Bioengineering, School of Engineering, Ecole Polytechnique Fédérale de Lausanne (EPFL), Lausanne, Switzerland. [3]Center for Neuroprosthetics and Brain Mind Institute, School of Life Sciences, Ecole Polytechnique Fédérale de Lausanne (EPFL), Lausanne, Switzerland. [4]Department of Clinical Neuroscience, Lausanne University Hospital (CHUV) and University of Lausanne (UNIL), Switzerland. [5]Defitech Center for Interventional Neurotherapies (.NeuroRestore), EPFL/CHUV/UNIL, Lausanne, Switzerland. [6]Bertarelli Foundation Chair in Neuroprosthetic Technology, Center for Neuroprosthetics, Institute of Electrical and MicroEngineering and Institute of Bioengineering, Ecole Polytechnique Fédérale de Lausanne (EPFL), Lausanne, Switzerland.
*Corresponding author. Email: gregoire.courtine@epfl.ch (G.C.); silvestro.micera@santannapisa.it (S.M.)
†These authors contributed equally to this work.
‡These authors contributed equally to this work.

RESULTS

Design of the neurorobotic platform

We first determined the key advantages of neurorobotic systems to study, assess, and restore upper limb movements, with the aim to translate these features into design specifications for the neurorobotic platform. We isolated five key features (Fig. 1).

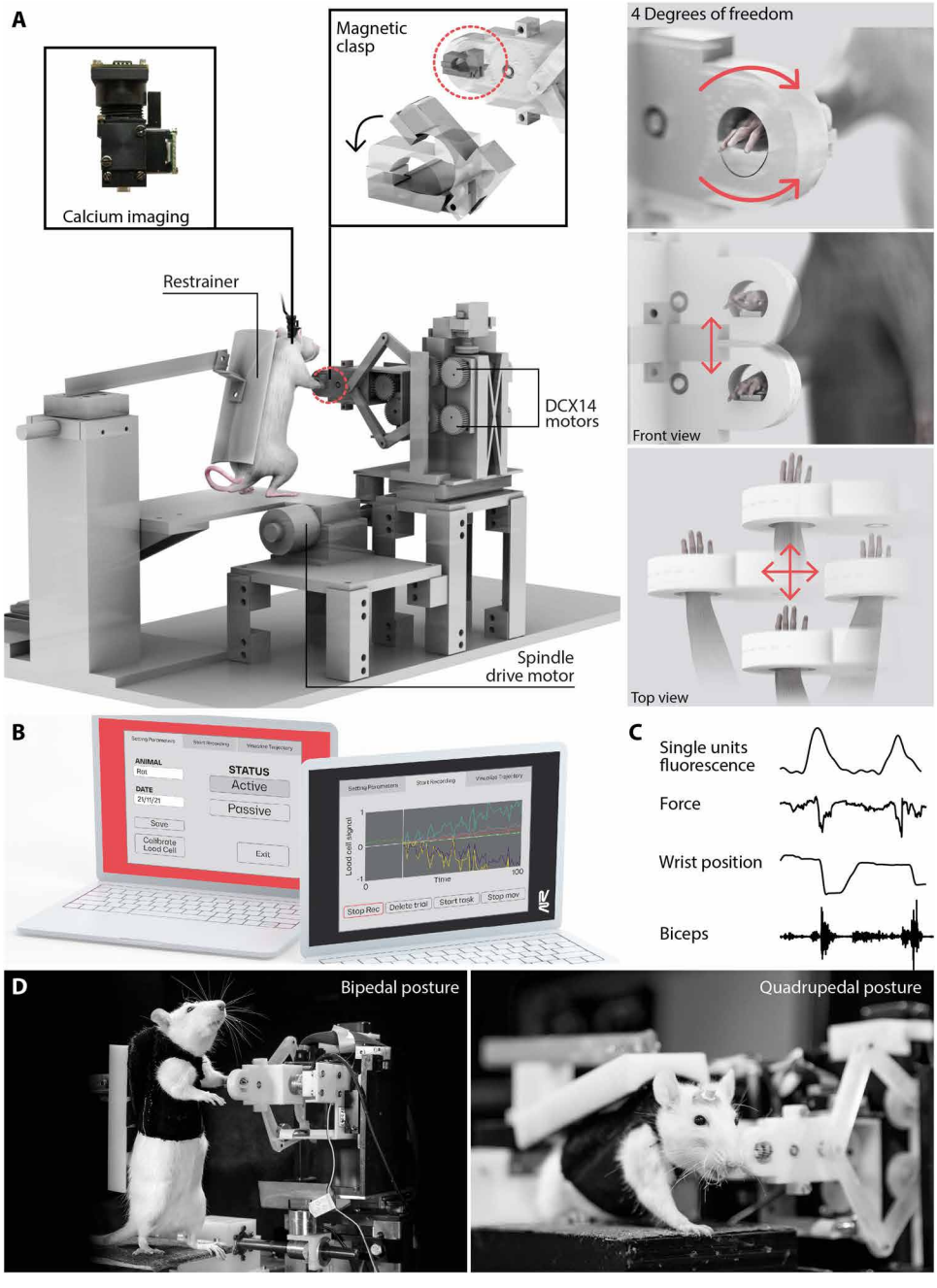

Fig. 1. The features of the preclinical neurorobotic platform. (**A**) 3D rendering of the mechanical structure of the R-Bot, emphasizing the four DOFs, with close-up views of the magnetic clasp to attach the paw to the R-Bot and to enable pronation and supination movements of the wrist. (**B**) LabVIEW GUI of the robotic device demonstrating a window for setting various parameters before recordings and a window for real-time data visualization. (**C**) Acquisition of multiple modalities, including neural recordings, kinetics, kinematics, and EMG activity from muscles. (**D**) Interaction of the rat with the robotic platform in bipedal (left) and quadrupedal (right) posture.

The first key feature involved the establishment of experimental conditions that enable the execution of natural upper limb movements. For example, the gold-standard single-pellet reaching task requires upper limb movements in a three-dimensional (3D) workspace combined with supination and pronation of the wrist (*23*). To permit such movements, we conceived a robotic interface consisting of an end effector operating over the four necessary DOFs. We termed this robotic interface the R-Bot (Fig. 1A).

The second key feature required the conception of a robotic system that enables movement as naturally as possible. However, the system must incorporate comfortable and reliable fixations that interface the limb with the apparatus to support adaptive manipulations of movement execution. For this purpose, we designed a sponge-lined clasp that comfortably secures the wrist of the rat to the end effector of the R-Bot (Fig. 1A).

The third key feature involved user-defined assistance of upper limb movement in each DOF. Concretely, the robotic interface must offer the possibility to enable completely passive movements, fully active movements, or a mixture of both along specific DOFs. For this purpose, we actuated the end effector of the R-Bot using four motors with individual high-resolution encoders. We inserted a miniaturized six-axis load cell in the gear mechanisms that allowed real-time measurement of force and torque at the end effector along six DOFs (fig. S1). This configuration enabled graded control over the relative assistance of upper limb movements along unconstrained, partially constrained, or fully constrained trajectories of the end effector (Fig. 1B).

The fourth key feature consisted of integrating recordings of movement features and neural activity with as many modalities as possible. For this purpose, we embedded the R-Bot into a versatile environment that enabled monitoring of kinetic and kinematic parameters, muscle activity, and neural signals without the need for additional constraints, such as a head fixation apparatus (Fig. 1C and fig. S1).

The fifth key feature focused on the advantages of allowing conditions that are potentially artificial for rats but that are relevant to develop therapies for humans. For example, our previously developed multidirectional body weight support interface enabled both quadrupedal and bipedal locomotion (*22*).

Albeit artificial, the bipedal posture abolished the contribution of upper limbs, thus restricting movement components to the studied lower limbs (*24*). Similarly, we reasoned that the difficulty to maintain quadrupedal posture after neurological disorders may affect the ability of rats to execute upper limb movements or may even favor compensatory contribution of the hindlimbs. Consequently, we designed a versatile support system that allowed us to manipulate the postural orientation and balance constraints during the execution of upper limb movements (Fig. 1D).

We synthetized this analysis into a neurorobotic platform that leverages each of these five key features. In the next sections, we sought to validate each of these five features experimentally and to illustrate how these features provide an instrumental environment to quantify and understand recovery from spinal cord injury (SCI), implement neurorehabilitation paradigms, and develop new neuroprosthetic therapies.

Natural movement execution (feature 1)

We first intended to illustrate the relevance of the four DOFs for the execution of natural upper limb movements in rats. We trained rats to retrieve food pellets using the gold-standard paradigm for upper limb movement assessments in rodents (*23*). This retrieval involved a well-coordinated pattern of upper limb muscle recruitment that produced a stereotyped 3D trajectory of the wrist combined with modest pronation of the wrist (Fig. 2A).

We then secured the wrist within the clasp and recorded the rats while they performed the retrieval (movie S1). The four DOFs enabled the production of 3D trajectories that resembled the natural trajectories of the wrist and involved comparable patterns of muscle activity (Fig. 2, B and C). This similarity was in stark contrast to the trajectories and muscle activity observed when retrieval movements were restricted to one DOF (Fig. 2, B and C).

To identify the more salient differences between both conditions, we leveraged the multimodal recording capacities of the neurorobotic platform. Concretely, we established an automated computational pipeline based on principal

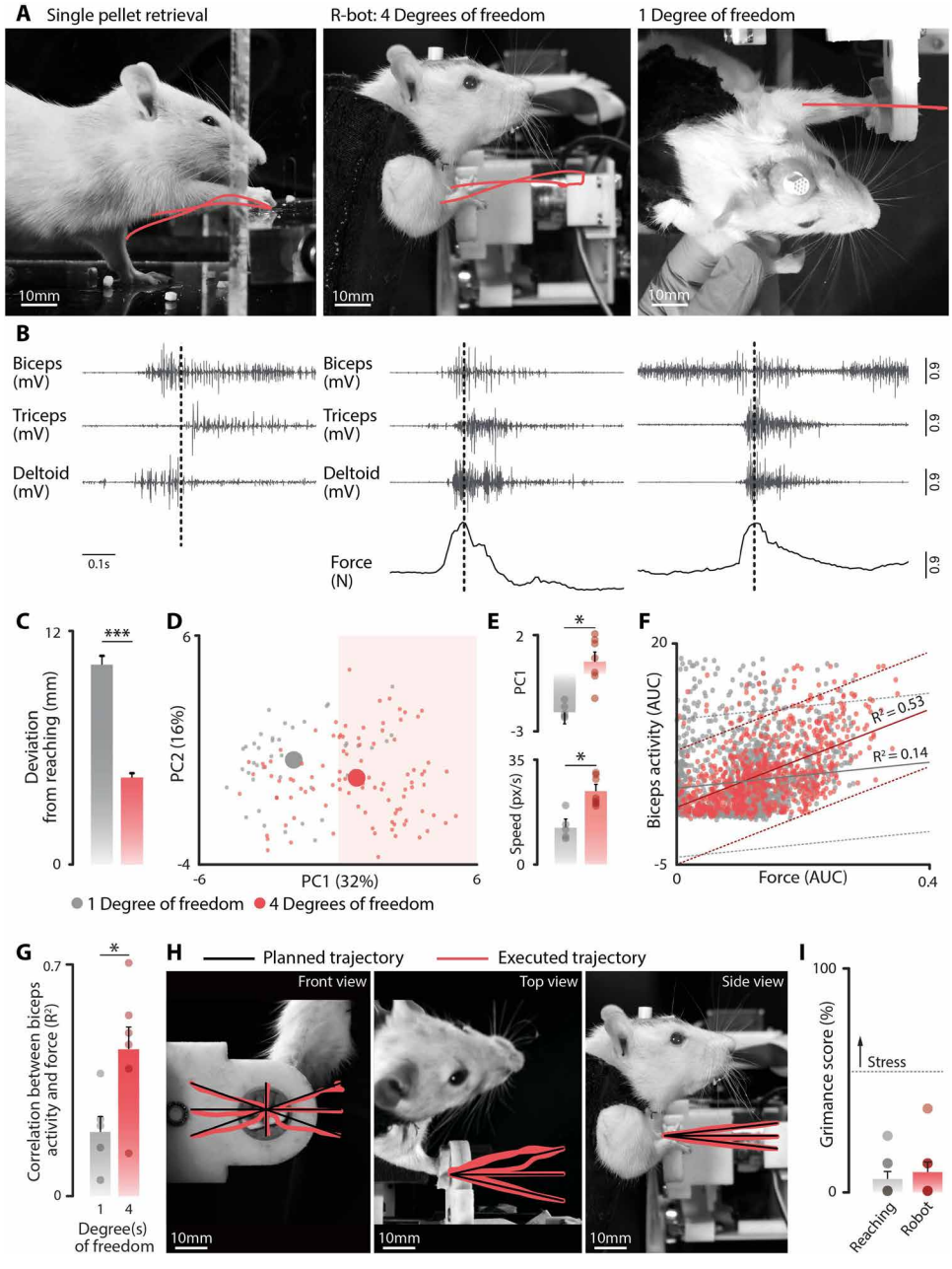

Fig. 2. Natural trajectories and precise control of movement execution. (**A**) Photographs with superimposed wrist trajectories underlying natural reaching behavior (left) and executions attached to the R-bot with four DOFs (middle) or only one DOF (right). (**B**) Representative recordings of muscle activity underlying each of the executions illustrated in (A) and force produced. (**C**) Bar plot reporting an average deviation from a natural reaching trajectory during execution with one versus four DOFs ($n = 50$ trials). (**D**) Representation of single executions in the denoised space created by the first two PCs. Each dot represents an execution, whereas large dots are averaged for a condition [measured across five (one DOF) or seven (four DOFs) recording days in $n = 2$ rats]. (**E**) Bar plot reporting scores on PC1, which segregates executions with one versus four DOFs. The second bar plot reports the mean speed of executions (px, pixel), which is one of the variables correlating with PC1. (**F**) Plot showing a representative correlation between the biceps activity and the produced force, evaluated in 200-ms time bins. (**G**) Correlation between the biceps activity and the produced force [measured across five (one DOF) or seven (four DOFs) recording days in $n = 2$ rats]. (**H**) The fixation of the wrist to the end effector via a cushioned magnetic clasp allows precise control of any user-defined trajectory within the 3D working space. (**I**) Bar plot reporting the grimace scores, showing that the robot does not induce discomfort or stress. For all bar plots, data are presented as means ± SEM; $^{*}P < 0.05$ and $^{***}P < 0.001$ (unpaired *t* test). AUC, area under curve.

component (PC) analysis that not only quantified performance but also uncovered the variables responsible for differences between experimental conditions (fig. S2). We first calculated various parameters from kinematic, kinetic, and muscle activity measurements (n = 32 parameters; table S1) and then subjected these parameters to a PC analysis. This unbiased assessment produced synthetic variables that segregated trajectories performed within the full 3D space and unconstrained within the four DOFs versus those strictly constrained within just a single DOF (PC1, $P < 0.05$; explained variance, 32%; Fig. 2, D and E).

The biceps muscle is responsible for elbow flexion, and accordingly, the activity of this muscle correlated with force production during retrievals when movement was unconstrained (Fig. 2, F and G). This similarity contrasted with the strong coactivation of muscles when the trajectory was constrained to one DOF. In this scenario, the activity of the biceps muscles no longer correlated with force production (Fig. 2, F and G). These results not only show that the R-Bot enables natural movement execution but also exemplify the importance of 3D trajectories and wrist pronation/supination movements to enable natural upper limb movement in rats.

Wrist fixation enables precise control over upper limb trajectories (feature 2)

We next evaluated whether the attachment of the wrist to the R-Bot within the clasp supported the production of versatile, user-defined wrist trajectories within the 3D workspace. We programmed the R-Bot to impose simple or complex wrist trajectories that covered the entire 3D workspace of the upper limb. The R-Bot was able to guide the wrist through the planned trajectories with high accuracy (Fig. 2H). The same results were obtained when the R-Bot imposed the trajectories with velocity profiles that obeyed or violated the two-third power law of upper limb movements (fig. S3).

We then used the grimace scoring system (*25*) to evaluate whether this potentially unnatural attachment induced discomfort or stress. None of the tested rats exhibited signs of discomfort, pain, or deviation from their natural behavior during the imposed movements of the wrist (Fig. 2I and movie S1).

User-defined assistance of upper limb movement (feature 3)

We then sought to demonstrate the ability of the R-Bot to impose the trajectories of the wrist recorded during natural retrievals and tested the influence of this imposed behavior on the kinetic, kinematic, and muscle activity of the rats. We transferred the 3D coordinates and velocity profiles of the average wrist trajectories measured during natural retrievals to the controller of the R-Bot and then recorded rats during fully assisted or unassisted retrievals with the upper limb attached to the R-Bot (Fig. 3, A and B, and movie S1).

The application of our automated computational analysis pipeline segregated trajectories associated with fully assisted versus unassisted executions (PC1, $P < 0.001$; explained variance, 29%; Fig. 3, C and D). To identify the variables that explained differences between both executions, we extracted the parameters that correlated highly with PC1 (fig. S3). We found that PC1 was near exclusively correlated with parameters related to the kinetic of movement. For example, rats produced fivefold superior levels of forces during unassisted compared with fully assisted retrievals (Fig. 3E and fig. S3). Instead, kinematic parameters loaded poorly on PC1, as expected based on the encoding of natural trajectories in the spatial and velocity profiles of fully assisted upper limb movements (Fig. 3A and fig. S3).

We reasoned that this superior force production must be linked to larger levels of muscle activity during unassisted compared with fully assisted retrievals. We detected a linear correlation between the peak force production and the amplitude of biceps muscle activity during unassisted retrievals ($R^2 = 0.52$, $P < 0.001$; Fig. 3, F to H). This relationship vanished during fully assisted retrievals ($R^2 = 0.12$, $P > 0.1$). However, muscles were not quiescent. Upper limb muscles displayed substantial levels of activity, but the recruitment

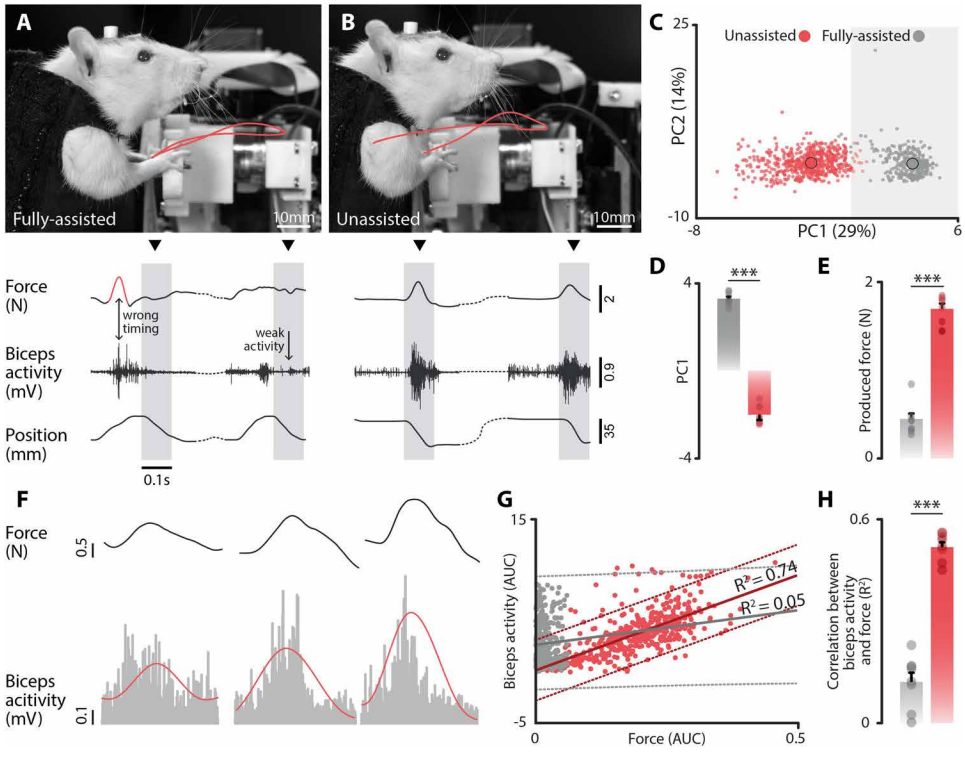

Fig. 3. Biomechanical features of unassisted and fully assisted movements. (**A**) Trajectories of fully assisted movement and (**B**) unassisted movement are plotted onto photographs of these executions. Concurrent recordings of biceps activity, produced force, and wrist position are shown during these executions. (**C**) Representation of fully assisted versus unassisted movements in the PC space (n = 8 rats). (**D**) Bar plot reporting the mean scores on PC1. (**E**) Bar plot reporting the mean produced force, which was one of the variables correlating with PC1. Data are presented as means ± SEM; ***$P < 0.001$ (RM ANOVA, Tukey's post hoc test). (**F**) Representative force peaks with their corresponding biceps activity (gray, raw data; red, envelope). (**G**) Plots showing a representative correlation between the biceps activity and the produced force, evaluated in 200-ms time bins. (**H**) Correlation between the biceps activity and the produced force (n = 8 rats). Data are presented as means ± SEM; ***$P < 0.001$ (Kruskal-Wallis test).

of these muscles was no longer synchronized with the trajectories (Fig. 3A and fig. S3).

These results not only showed the ability of the R-Bot to impose upper limb trajectories with user-defined spatial and velocity properties but also exposed substantial differences in the kinetic and muscle activity parameters during unassisted versus fully assisted performance of otherwise kinematically comparable upper limb movements.

Voluntary force production engages corticospinal tract neurons (feature 4)

These results suggested that, as expected, the brain is more involved in the production of unassisted movements compared with fully assisted movements. We sought to take advantage of this logical hypothesis to ask whether the multimodal recording capabilities of the neurorobotic platform provide the tools to test this interpretation.

We equipped the neurorobotic platform with additional hardware that enabled the recording of neural activity via live calcium imaging (Fig. 4A and fig. S4). We aimed to monitor the activity of corticospinal tract neurons that establish synaptic projections into the cervical segments containing biceps motor neurons. Intramuscular injections of a retrograde tracer into the biceps showed that motor neurons innervating this muscle are located within C4/C5 segments (fig. S4). To express the calcium indicator GCaMP6m in corticospinal tract neurons projecting to these cervical segments,

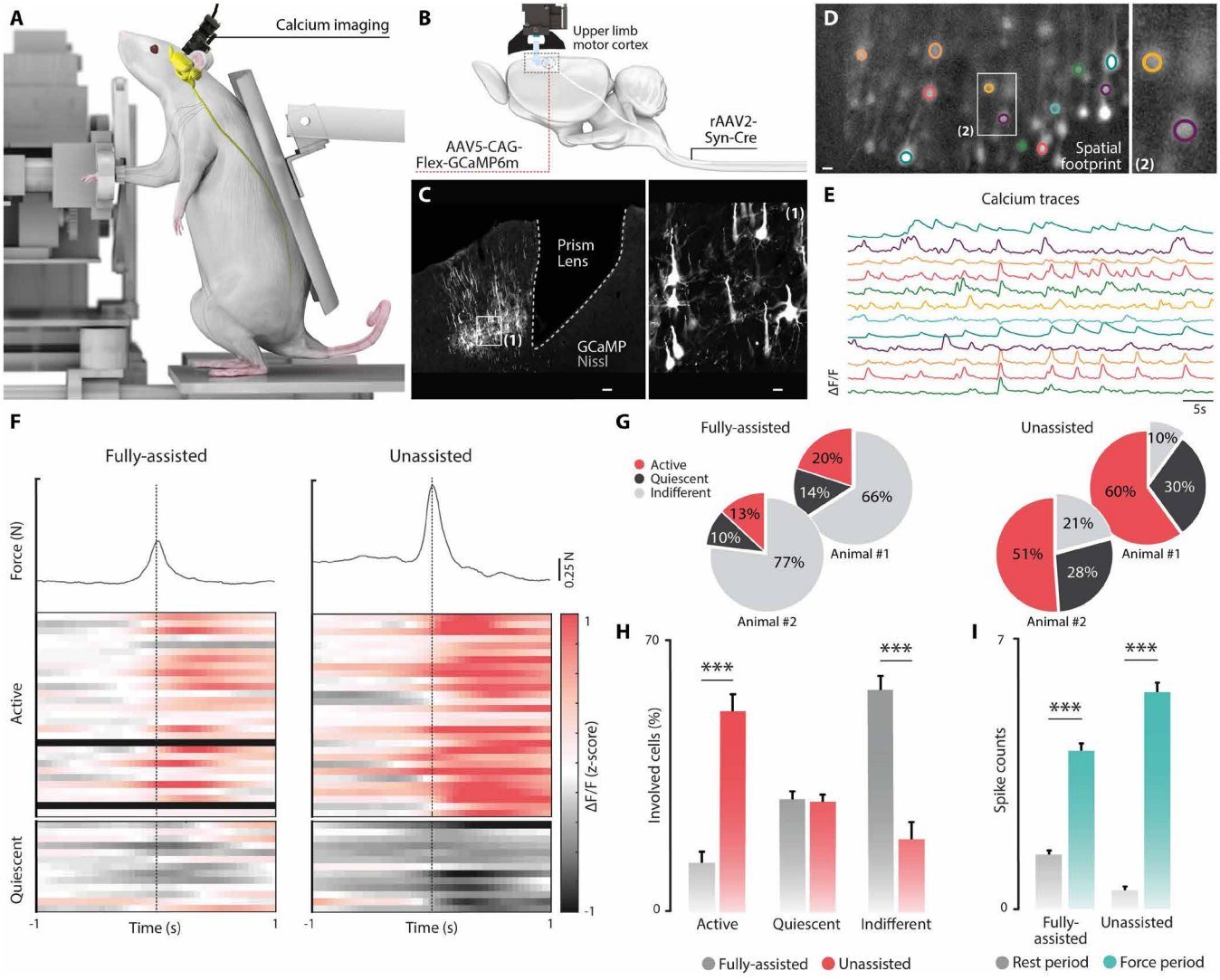

Fig. 4. Corticospinal tract neuron dynamics during unassisted and fully assisted movements. (**A**) Schematic of experimental paradigm. (**B**) Intersectional virus strategy to express GCaMP6m in corticospinal tract neurons projecting to cervical segments. A miniscope is mounted on a head plate to image calcium activity during retrievals. (**C**) GCaMP6m^{ON} neurons adjacent to the position of the implanted prism lens. Scale bars, 200 μm; inset (1), 20 μm. (**D**) Representative example of recorded neurons located in the microscope field of view, including neurons highlighted with colors (scale bar, 50 μm) (**E**) whose calcium traces are displayed during successive retrievals. (**F**) Continuous mean activity of individual neurons ($\Delta F/F$ *z* score) when aligned with force peaks (dashed line) occurring during fully assisted or unassisted movements. (**G**) Camembert plots reporting the relative proportion of active, quiescent, or indiscriminately active neurons compared with baseline during unassisted and fully assisted movements for the two recorded rats. (**H**) Bar plot reporting the mean ($n = 5$ days of recording) percentage of neurons for each established class during fully assisted versus unassisted movements. (**I**) Mean ($n = 5$ days of recording) frequency of Ca^{2+} events (spike count) during rest and force production periods (1-s duration) of fully assisted and unassisted movements. For all bar plots, data are presented as means ± SEM; ***$P < 0.001$ (Kruskal-Wallis test).

we infused rAAV2-hSyn-Cre into the C5/C6 segments coupled with Cre-dependent infusions of AAV5-CAG-flex-GCaMP6m into the caudal forelimb area (CFA) of the motor cortex (Fig. 4B and fig. S4). To record calcium activity, we chronically implanted a prism lens into the CFA (Fig. 4, C to E), which we interfaced with the ultralight Inscopix miniscope (Fig. 4, A and B, and fig. S4).

The production of forces during unassisted retrievals involved the recruitment of the biceps muscle, which was systematically paralleled by a robust increase or decrease in calcium activity of numerous corticospinal tract neurons (Fig. 4F and fig. S4). Neural classification analysis (*26*) based on correlations with the occurrence of a force peak (fig. S4) revealed that 51 to 60% of the recorded neurons showed a significant increase in activity during retrievals (active neurons), 28 to 30% exhibited a significant decrease (quiescent neurons), and 10 to 21% were indiscriminately active (indiscriminate neurons) (Fig. 4G).

Fully assisted retrievals also involved peak force–related changes in calcium activity of numerous corticospinal tract neurons (Fig. 4F). Compared with unassisted retrievals, however, there was a fourfold reduction in the number of active neurons, because most neurons became indiscriminately active during fully assisted retrievals (Fig. 4G). Although the number of active neurons depended on the presence or absence of movement assistance, quantification of calcium events revealed that all neurons classified as active displayed a robust firing during force production (Fig. 4, H and I, and fig. S4).

These results confirm our hypothesis that the cortical neurons projecting to the cervical spinal cord are markedly more engaged in retrievals when the movement is unassisted compared with fully assisted. Such findings illustrate the value of the neurorobotic platform to monitor neuron-specific activity underlying well-controlled motor executions.

Artificial postures establish relevant experimental conditions (feature 5)

We sought to illustrate whether manipulating the postural orientation during retrieval would provide relevant experimental advantages to evaluate upper limb movements in rats. Rats were trained to perform retrievals in a natural quadrupedal posture (Fig. 5A) or artificial bipedal posture while partially supported in a body weight support system (Fig. 5B). PC analysis distinguished differences in the characteristics of movement execution when performing the task quadrupedally versus bipedally (Fig. 5, C and D). Specifically, rats performed the task more frequently, at higher speed, and with superior peak force production when they executed the retrieval in a bipedal posture compared with a quadrupedal posture (Fig. 5, E to H). This result illustrates the relevance of the artificial bipedal posture to maximize the engagement of rats in the performance of upper limb movements and isolate the participation of upper limb versus lower limb components.

Taken together, the results of this series of experiments validate the relevance of the five key features that steered the design of the preclinical neurorobotic platform. We next aimed to demonstrate the ability of this platform to quantify recovery from neurological deficits, enable neurorehabilitation, and support therapy development.

Longitudinal quantification of recovery from SCI

We aimed to show the ability of the neurorobotic platform to quantify deficits in upper limb movements and to uncover mechanisms of recovery from neurological impairment. We selected a contusion

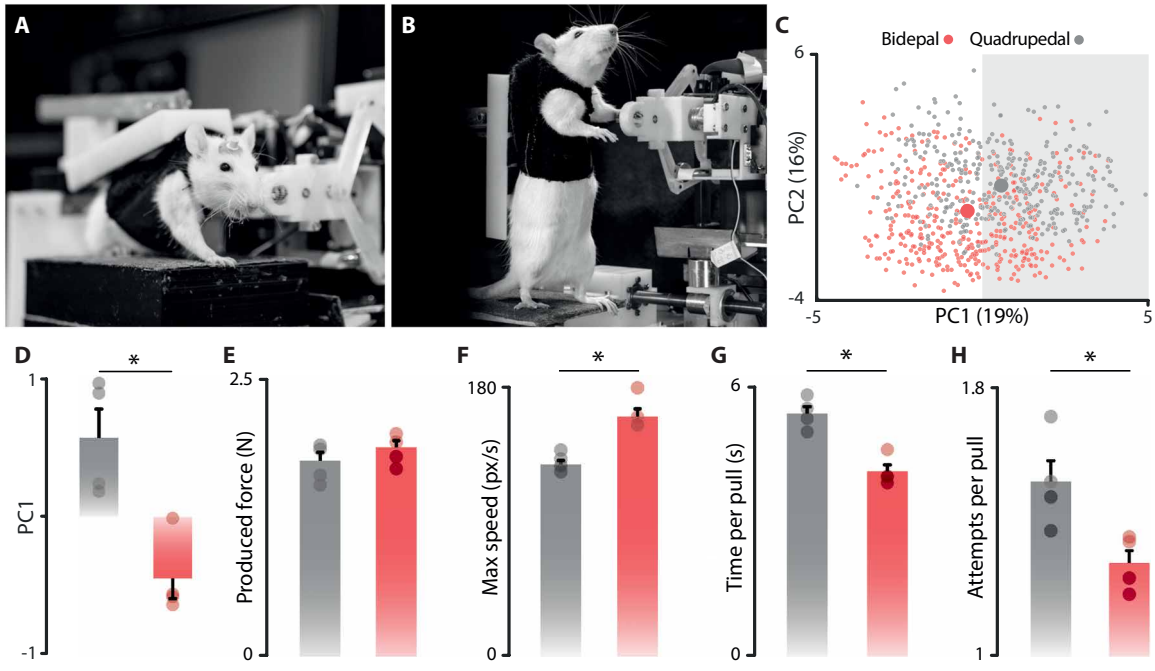

Fig. 5. Artificial posture provides superior experimental conditions. (**A** and **B**) Interaction of the rat with the robotic platform in bipedal (A) and quadrupedal (B) postures. (**C**) Representation of retrievals under bipedal versus quadrupedal posture in the PC space ($n = 4$ rats). (**D**) Bar plot reporting score on PC1 for bipedal versus quadrupedal postures. (**E** to **H**) Variables that correlated with PC1 and thus accounted for the most pronounced differences between the retrievals with bipedal versus quadrupedal postures. For all bar plots, data are presented as means ± SEM; *$P < 0.05$ (Mann-Whitney test).

SCI to model clinically relevant upper limb impairments because this type of spinal cord damage reproduces the neuropathology most frequently observed in humans (*27*). To induce severe contusions, we delivered robotically controlled impacts onto the C5 spinal segment. To minimize detrimental effects on animal welfare, we restricted the contusion to the hemicord involved in the control of the dominant upper limb (fig. S5). Light sheet microscopy (*28*) of cleared brain–spinal cord tissues revealed that the contusion disrupted the integrity of the entire targeted hemicord (47.5 ± 3.3%; Fig. 6, A and B, and fig. S5), leading to the interruption of corticospinal tract projections (Fig. 6A).

The SCI permanently abolished skilled motor performance. For example, the gold-standard single-pellet task failed to capture functional recovery (fig. S5). Instead, the rats progressively recovered

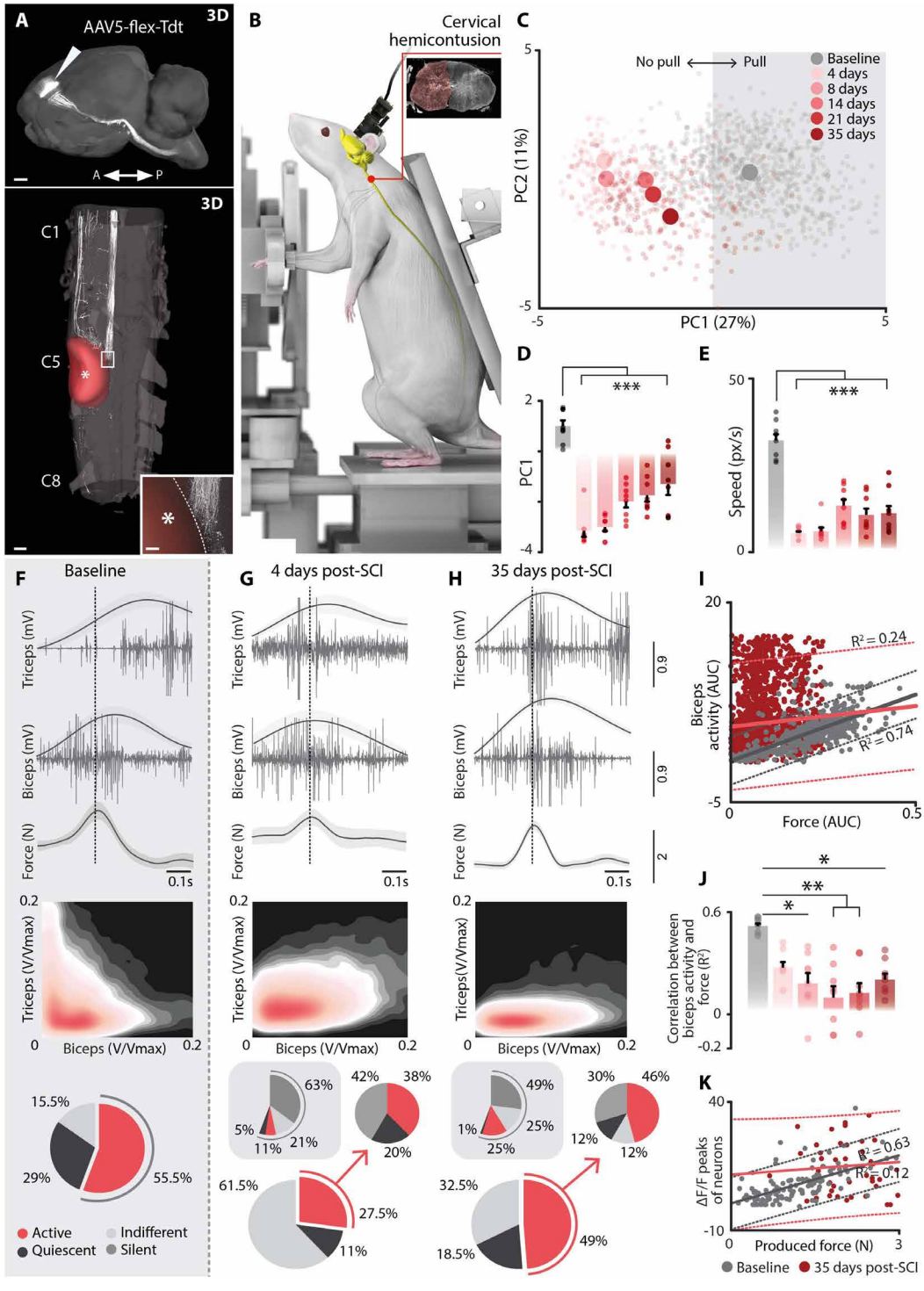

Fig. 6. Longitudinal quantification of functional recovery. (**A**) Whole brain–spinal cord visualization of corticospinal tract neurons and their projections to the cervical injured spinal cord using CLARITY. Scale bars, 2 mm (brain), 1 mm (spinal cord), and 250 μm (inset of lesion). (**B**) Schematic of the experimental paradigm. (**C**) Representation of retrievals in the PC space, before and over the time course of recovery from the SCI ($n = 8$ rats). (**D**) Bar plot reporting the mean scores on PC1 for the different time points. (**E**) Bar plot reporting the mean speed of execution, because this parameter strongly correlated with PC1. Data are presented as means ± SEM; ***$P < 0.001$ (RM ANOVA, Tukey's post hoc test). (**F** to **H**) Representative examples from a single rat of the averaged envelope of the triceps and biceps aligned to force peaks, before (F), 4 days (G), and 35 days (H) after injury. Error shading indicates the SE across various force peaks. The plots in the middle report the probability density distribution between biceps and triceps. L shapes indicated alternation between the activities of these antagonist muscles, while other geometric shapes emphasize coactivation. The camembert plots report the proportion of active, quiescent, indiscriminately active, or silent neurons compared with baseline. Insets in gray boxes report what neurons classified as active at baseline become after injury. Second insets report the original baseline classification of neurons classified as active after injury ($n = 2$ rats). (**I**) Correlation between biceps activity and the produced force before (gray) and after (red) the SCI, evaluated in 200-ms time bins. (**J**) Plot reporting the mean ($n = 8$ rats) correlation coefficient (R^2) for the relationship shown in (I) for one rat. Data are presented as means ± SEM; *$P < 0.05$ and **$P < 0.01$ (RM ANOVA, Tukey's post hoc test). (**K**) Correlation between the peak value of produced force and the overall neuronal activity combining all the neurons exhibiting Ca^{2+} events during the corresponding interval.

the ability to perform basic retrievals in the neurorobotic platform. To quantify this recovery, we applied the automated computational pipeline on the multimodal data that were recorded weekly over a period of 5 weeks after the injury. PC1 captured the relative degree of impairments compared with preinjury (Fig. 6, C to E, and fig. S5). Therefore, scores on PC1 quantified the gradual yet partial recovery of upper limb retrieval function (Fig. 6D). Instead, assessments during fully assisted movements failed to capture the extent of the impairment and recovery (fig. S5).

We then studied the neurobiomechanical features that enabled the partial recovery of unassisted retrievals. To identify these features, we extracted the parameters that correlated with PC1, also termed syndromic outcomes (*29*). We found that improvements were linked to the near-complete recovery of peak force production, albeit the mean force levels remained lower than before the injury (fig. S5). This inability to produce sustained forces was reflected in abnormal patterns of muscle activity. Before the injury, retrievals involved the alternating recruitment of the biceps and triceps muscles (Fig. 6F). The rats failed to regain the ability to produce this sequence of muscle recruitment patterns and instead exhibited a pronounced coactivation of these muscles throughout the period of recovery (Fig. 6, F to H). This coactivation abolished the correlation between the production of force and activity of the biceps muscle (Fig. 6, I and J).

We thus asked whether this disruption was reflected in a similar alteration in the encoding of retrievals in corticospinal tract neurons. We monitored calcium events in the same population of cortical neurons projecting to the cervical segments before and throughout recovery from the SCI that interrupted these projections (Fig. 6A). This interruption led to an immediate disengagement of corticospinal tract neurons in movement production. Whereas most of the recorded neurons were classified as active before the injury, more than half of these cells became completely silent (Fig. 6, F to H). The number of active neurons increased during recovery, albeit the relative number of active neurons never reached the same level as before the injury (Fig. 6, F to H). The neurons that became gradually active after the injury primarily originated from a population of cells that had been silent before injury (Fig. 6, G and H). Throughout recovery, however, the amplitude of calcium events in active neurons no longer correlated with the level of force production (Fig. 6K). This gradual reorganization of cortical activity suggested that a new class of neurons became involved in movement execution to compensate for the interruption of projections from cortical neurons to their targets in the spinal cord. These results show that the neurorobotic platform is instrumental not only to quantify the gradual recovery of upper limb motor functions from an SCI but also to uncover the neurobiomechanical features and neural mechanisms that underlie this recovery.

Robot-assisted neurorehabilitation after SCI

We next sought to evaluate whether the neurorobotic platform establishes an advantageous environment to deliver neurorehabilitation interventions. Rats with a contusion SCI followed a daily neurorehabilitation program that involved a personalized combination of fully assisted and unassisted retrievals. The instrumentation of the neurorobotic platform enabled daily automated monitoring of the gradual motor recovery throughout the period of neurorehabilitation (Fig. 7, A to C). Our computational analysis pipeline quantified this progressive recovery of force production, which contrasted to the limited recovery observed in untrained rats (Fig. 7D).

We then sought to document the additional advantages of the robot-assisted training paradigm to monitor recovery during neurorehabilitation. For this purpose, we tested rats that underwent a more conventional rehabilitation program based on gold-standard pellet retrieval. Whereas the neurorobotic platform captured early recovery of upper limb motor functions, we failed to detect an improvement in the pellet retrieval tasks during the first weeks after the injury (fig. S5).

Although the robotic interface was not designed to establish optimized conditions for neurorehabilitation, this paradigm provides well-controlled and quantified conditions that promote the engagement of rats into rehabilitation early after injury. Under these conditions, rats not only exhibited superior recovery compared with untrained rats but also showed early signs of recovery that could not be detected with more conventional rehabilitation paradigms (Fig. 7E). We concluded that the neurorobotic platform paradigm presents numerous experimental advantages to study the mechanisms underlying recovery from neurorehabilitation interventions.

Advantageous environment for therapy development

Last, we aimed to demonstrate that the wrist attachment and artificial bipedal posture provide advantageous conditions to develop therapies for restoring upper limb functions. We previously showed that the delivery of epidural electrical stimulation (EES) over the lumbar spinal cord restored walking after paralysis due to an SCI (*30*). EES recruits large-diameter afferent fibers within the dorsal roots, which leads to the modulation of motor neurons located in the spinal segment innervated by the recruited root (*31*–*33*). In turn, activity-dependent motor neuron activation patterns can be elaborated by targeting individual dorsal roots with the appropriate timing (*33*, *34*). Here, we hypothesized that activity-dependent modulation of cervical motor neurons with EES can also improve upper limb motor functions after SCI.

We first injected anatomical tracers into muscles to identify the location of motor neurons innervating the biceps and triceps muscles, which are the main actuators of reaching and retrieval functions. We found that these motor neurons are located in distinct cervical segments, suggesting that these cells could be modulated independently by targeting their respective dorsal roots (Fig. 8A). To test this possibility, we identified the optimal location of electrodes based on measurements of dorsal root topology. We then configured electronic dura mater (e-dura) implants (*35*) with an arrangement of electrodes that covered the cervical hemicord innervated by the targeted dorsal roots (Fig. 8B and fig. S6).

Rats underwent a severe cervical hemicontusion SCI that abolished reach and retrieval functions. In the same surgery, the e-dura implant was positioned over the targeted dorsal roots. The SCI led to severe deficits in upper limb movements and postural control. Accordingly, the configuration of EES protocols could not be conducted in freely behaving rats during the first days or even weeks after injury. Under these circumstances, the neurorobotic platform became critical to enable these configurations. First, the attachment of the wrist to the end effector provided a level of support and assistance to the upper limbs that established appropriate conditions to map the relationships between EES parameters, muscle activation, and force production. Second, the rats could be constrained in a bipedal posture with a body weight support that minimized the impact of postural disturbances on the execution of upper limb

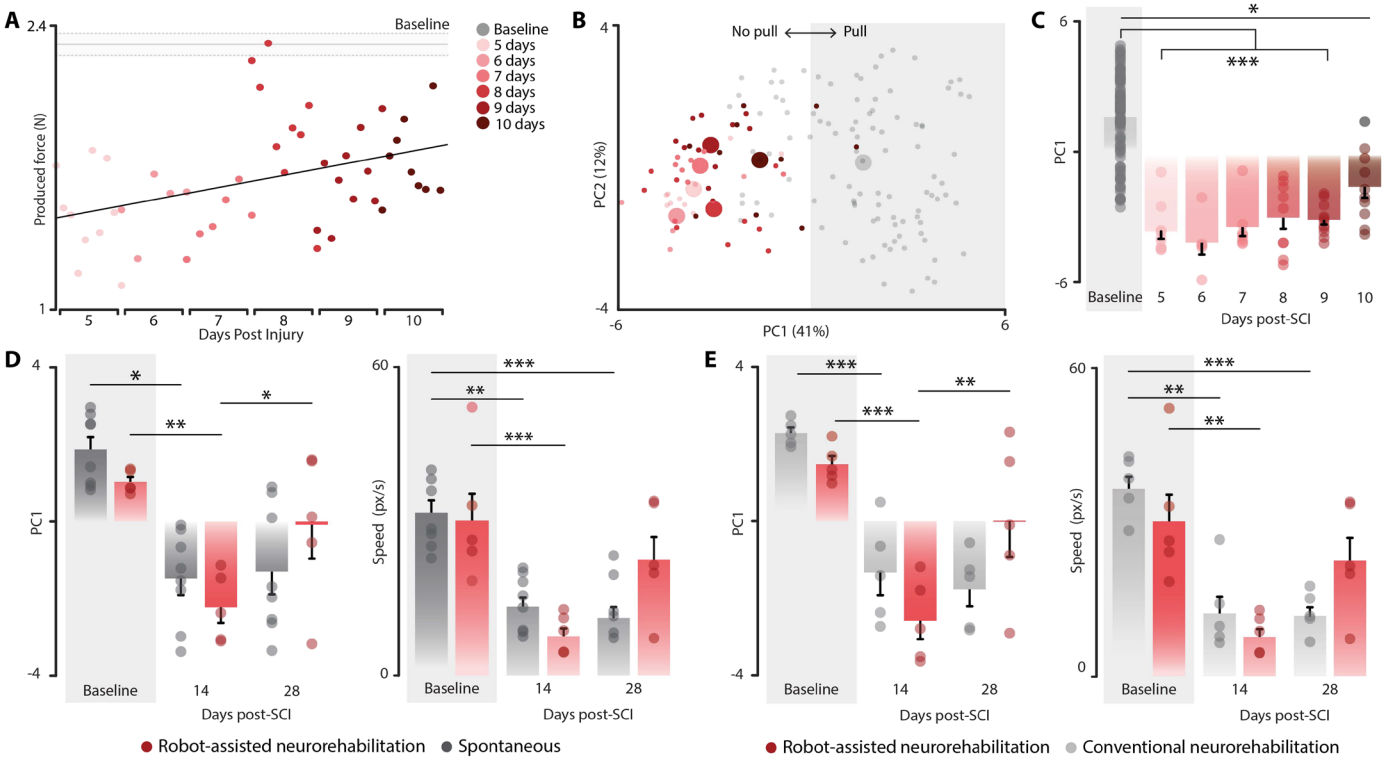

Fig. 7. Robot-assisted neurorehabilitation after cervical SCI. (**A**) Plot showing the evolution of the produced force over the course of daily neurorehabilitation sessions using automated assessments in a single representative animal. (**B**) Representation of retrievals in the PC space, before and over the daily neurorehabilitation after the SCI in the same representative animal. (**C**) Bar plot reporting scores on PC1 before and over the course of daily neurorehabilitation after the SCI. (**D**) Bar plots reporting scores on PC1 (left) and speed of retrievals (right) for rats that underwent daily robot-assisted neurorehabilitation ($n = 5$ rats) compared with rats that remained untrained (spontaneous recovery; $n = 8$ rats). (**E**) Bar plots reporting scores on PC1 (left) and speed of retrievals (right) for rats that underwent daily robot-assisted neurorehabilitation ($n = 5$ rats) compared with rats that followed a conventional neurorehabilitation program ($n = 5$ rats). For all bar plots, data are presented as means ± SEM; $^{*}P < 0.05$, $^{**}P < 0.01$, and $^{***}P < 0.001$ (two-way RM ANOVA, Tukey's post hoc test).

movements. Therefore, the neurorobotic platform provided an advantageous environment wherein numerous repetitions could be performed under reproducible, standardized, and well-controlled conditions as early as 1 day after SCI.

Leveraging the advantageous environment of the neurorobotic platform, we could establish a comprehensive mapping of the relationships between the location of EES and the recruitment of upper limb muscles within a single session. We thus obtained motor neuron activation maps that uncovered the relationship between each electrode/EES parameters and the activation of specific muscles (Fig. 8C). Compared with other electrodes, EES delivered through the electrode associated with the targeted muscle led to larger force production (Fig. 8, D and E).

We then implemented an algorithm that triggered EES bursts targeting triceps or biceps motor neurons based on the detection of the relevant muscle activity while the rats were attempting to perform reach or retrieval movements (Fig. 8F). This activity-dependent stimulation protocol enabled the production of significantly larger force than continuous stimulation (Fig. 8, G and H). The preclinical neurorobotic platform allowed us to demonstrate that activity-dependent control of EES augments the volitional activation of motor neurons innervating upper limb muscles, allowing rats with SCI to regain the ability to produce force.

DISCUSSION

We conceived, validated, and leveraged a preclinical robotic platform that allowed us to expose the importance of active movement to engage corticospinal tract neurons, quantify upper limb movement recovery after SCI, uncover neural mechanisms underlying this recovery, and personalize neurorehabilitation programs. We also illustrated how this platform can play an instrumental role in developing an implantable neuroprosthesis to restore upper limb movements after SCI. Central to all these achievements was the conception of a platform that incorporated key advantages of robotic environments for investigating movement recovery in preclinical models: well-controlled, standardized, quantified, and even artificial conditions that support the development of therapies for restoring motor control after neurological disorders.

Quantification of upper limb motor performance in preclinical models of neurological disorders is often restricted to success rates in single-pellet retrieval or to complex, time-consuming analyses of video recordings (*23*, *36*, *37*). Here, we endowed our preclinical neurorobotic platform with multimodal recording capabilities that allowed us to capture longitudinal changes in the neurobiomechanics of upper limb motor function after SCI. In addition, we established an automated computational pipeline that not only generates synthetic components providing an objective quantification of performance but

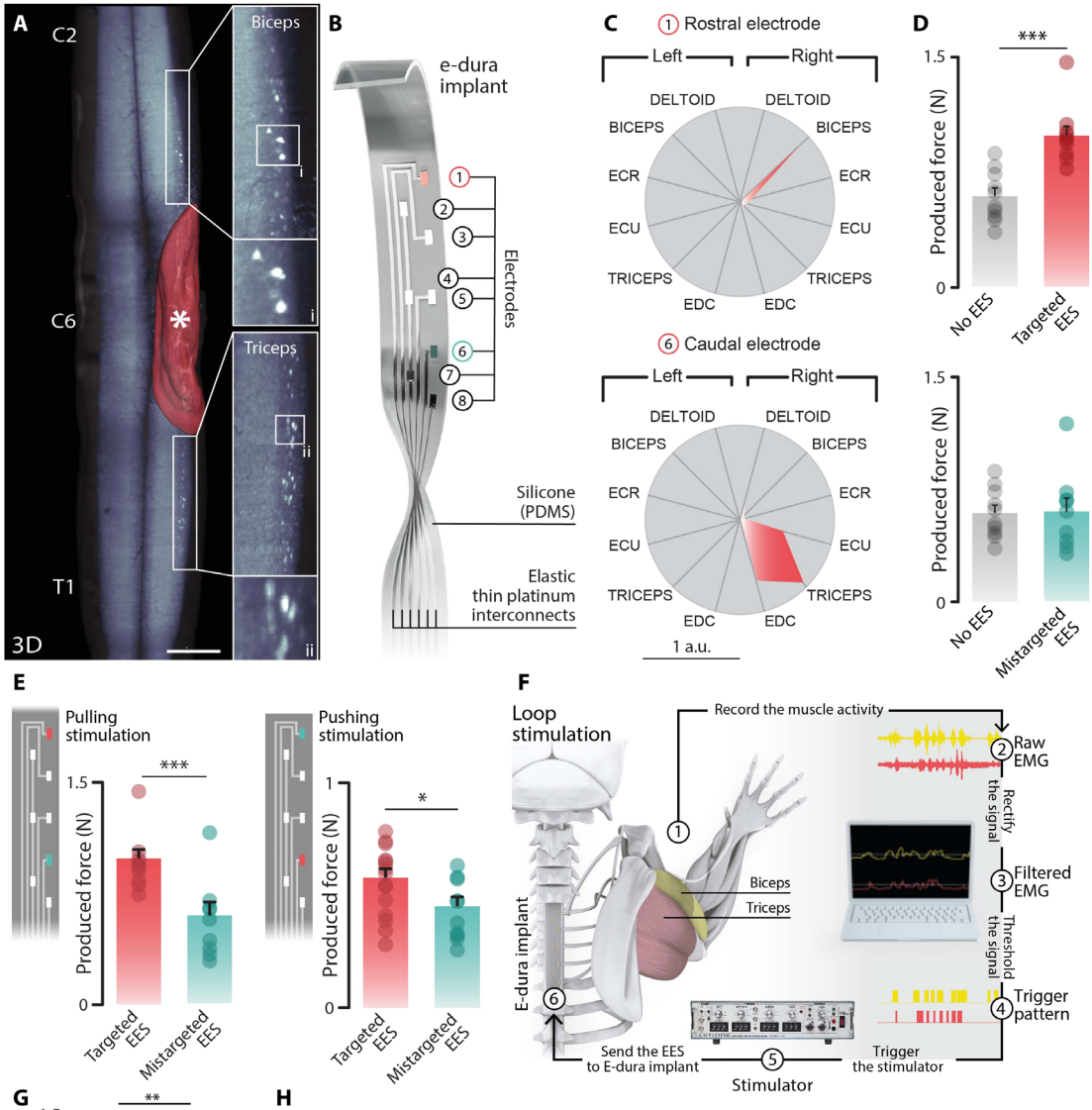

Fig. 8. Well-suited environment for therapy development. (**A**) uDisco clearing of FluoroRuby-traced motor neurons in the injured cervical spinal cord reveals the location of the biceps and triceps motor neuron pools. Scale bar, 1 mm. (**B**) A custom-designed e-dura implant allows selective targeting of specific motor neuron populations. (**C**) Polar plots showing the relative activation of each upper limb muscle with targeted EES (electrode 1 versus 6). ECR, extensor carpi radialis (wrist abduction); ECU, extensor carpi ulnaris (wrist adduction); EDC, extensor digitorum communis. a.u., arbitrary units. (**D**) Bar plots reporting the produced force without EES, with targeted EES (electrode targeting the appropriate muscle for the intended movement), and with mistargeted EES (electrode targeting an incorrect muscle). Data are presented as means ± SEM ($n = 8$ to 10 trials per condition in $n = 1$ rat); ***$P < 0.001$ (Student's t test). (**E**) Compared with mistargeted EES (green electrodes in scheme of arrays), EES delivered through the electrode (red) targeting the appropriate muscle for the desired movement (pulling or pushing) led to increased force production, as reported in bar plots. Data are presented as means ± SEM ($n = 8$ to 10 trials per condition, $n = 1$ rat per task); *$P < 0.05$ and ***$P < 0.001$ (Student's t test). (**F**) Schematic showing how detection of muscle activity triggers bursts of EES targeting the activated muscle. This activity-dependent stimulation protocol augments muscle activation. (**G**) Bar plots reporting the increased produced force during activity-dependent EES compared with continuous EES. Data are presented as means ± SEM ($n = 8$ to 10 trials per condition in $n = 1$ rat); **$P < 0.01$ (Student's t test). (**H**) Representative raw force, biceps muscle activity, and wrist position traces for each of the different stimulation protocols.

also identifies the specific ensemble of variables accounting for these performances. Comparable recordings and analyses can be readily implemented in humans, opening a pathway for translational syndromic outcomes across multiple fields of neurological research.

Activity-based therapies are common in medical practice for augmenting recovery from neurotrauma (*38*–*40*). These therapies are based on the fundamental principle that the repeated activation of circuits during neurorehabilitation triggers activity-dependent plasticity of

the activated circuits. This neuroplasticity improves functional recovery. Therefore, the efficacy of activity-based therapies logically correlates with the ability of neurorehabilitative interventions to engage the targeted circuits. The multimodal recording capabilities of the neurorobotic platform allowed us to demonstrate that, as expected, fully assisted movements do not require the engagement of the motor cortex in force production. This observation suggests that robot-assisted rehabilitative training with full assistance is unlikely to promote neuroplasticity of the critically important corticospinal tract.

Previous studies using functional imaging technologies in humans reported a comparable reduction of cortical activity during passive compared with active upper limb movements (*41*, *42*). Here, we demonstrate that this reduction of cortical activity is due to the specific disengagement of corticospinal tract neurons that project to spinal segments responsible for the execution of movement. This result reinforces the importance of creating neurorehabilitation conditions that maximize the engagement of the brain.

We previously exposed the mechanisms supporting this therapeutic framework. We designed two neurorehabilitation protocols that encouraged the participation of the brain or, instead, did not require the involvement of the brain. The first protocol required the rats to walk overground, which constrained the brain to send commands to the spinal cord to initiate and sustain walking. We compared this protocol with automated stepping on a treadmill, which did not require involvement of neuronal networks in the brain (*7*). We found that active locomotor training triggered the extensive growth of new connections throughout the brainstem and spinal cord (*7*, *43*), whereas passive step training only promoted neuroplasticity below the SCI. Accordingly, only rats trained under active conditions regained volitional control of locomotion in response to neurorehabilitation (*7*). These results showed that functional neuroplasticity of descending pathways requires conditions that foster the communication between circuits located above and below the SCI.

Robotic interfaces provide advantageous features to establish these conditions. For example, we show here that the preclinical robotic platform enabled the adaptation of rehabilitation conditions to the current capacities of the rats. This personalization allowed us to create paradigms that encouraged active participation of the rats in neurorehabilitation as early as a few days after injury. This early engagement in active training accelerated the recovery of upper limb functions compared with conventional rehabilitation procedures.

We also anticipate that the neurorobotic platform could support the development of new neurorehabilitation paradigms. For example, we showed that neurorobotic platforms enable the delivery of intensive, repeatable exercises that can be combined with activation (*43*–*45*) or inactivation (*14*) of relevant brain regions. Here, we only implemented basic rehabilitation protocols, but the versatility of the platform could support more complex learning paradigms that may be important to exploit the full potential of rehabilitation robotics to augment recovery (*5*, *33*, *39*, *46*).

Critical to enable the early participation of rats in neurorehabilitation was the artificial support conditions that compensated for the impaired postural control. Rats with severe SCI were not able to maintain a well-balanced posture, as necessary to perform retrievals. Therefore, the neurorobotic platform established artificial, yet instrumental, conditions to enable rats to engage in neurorehabilitation as early as possible.

The same principle supported the validation of the therapeutic concepts through which EES can modulate the activity of upper limb muscles after SCI. We created an artificial environment that allowed us to map the muscle responses to EES protocols under well-controlled conditions, with adequate postural support of the body and upper limbs and without confounding behavioral factors. We could thus establish a cartography of muscle responses to EES within a single mapping session.

We previously used the same principles to develop a lower limb neuroprosthesis. Specifically, we leveraged body support systems that enabled mice and rats with complete SCI to produce automated bipedal stepping on a treadmill (*22*, *47*). This artificial bipedal posture within the well-controlled treadmill environment allowed us to decipher the relationships between EES parameters and the modulation of otherwise paralyzed lower limb muscles (*30*). We translated this knowledge into spatiotemporal EES protocols that restored full weight–bearing locomotion in people with paralysis due to an SCI (*23*). Although rats did not recover natural locomotor functions, the understanding gained with the artificial experimental conditions was sufficient to develop an effective treatment for humans. Similarly, the rats did not recover natural upper limb functions, but the preclinical neurorobotic platform allowed us to validate key concepts of EES for the cervical spinal cord, thus paving the way toward applications of these concepts in humans. We surmise that many therapeutic interventions can benefit from being developed in conditions that are artificial for rats and not necessarily functional, but that are relevant to validate concepts and develop engineering framework for applications in humans.

Most of the existing manipulanda for rodents operate within a single DOF (*20*, *21*). These robotic platforms enable quantification of arm functions, but their simple mechanical structure is less appropriate to study motor learning and mechanisms of neurological recovery. To overcome this limitation, two platforms supporting planar movements (*18*, *48*) and one robotic interface enabling movement within a tridimensional workspace (*19*) have been previously designed. The ETH Pattus (*18*) assists wrist movements within a single plane while permitting pronation/supination of the wrist. The other platform (*48*) leverages a head restrainer to support wrist movement within a single plane while monitoring the underlying neuronal activity. The tridimensional robotic platform (*19*) integrates a three-revolute-prismatic-spherical structure to increase the back-drivability of the system within the entire workspace. Each of these platforms was designed to support specific experimental paradigms, with defined objectives. Consequently, these manipulanda are specialized and do not provide the same degree of versatility and adaptability as our neurorobotic platform to study motor control, assess neurological recovery, and develop treatments while allowing multifaceted assessments of neurobiomechanics and neuronal dynamics. Such assessments are critical to dissect the mechanisms of neurological recovery and thus develop new therapeutic strategies based on this understanding (*5*, *49*). Moreover, our robotic platform shares many key features with the systems that are used in clinical settings, such as operating within the entire workspace to support reaching functions during neurorehabilitation (*8*, *9*). These systems are frequently coupled with neuromuscular stimulation paradigms (*5*). Similarly, we coupled the robotic platform with activity-dependent EES to augment the recovery of reaching, illustrating a remarkable parallel between preclinical and clinical applications. Here, we designed a neurorobotic platform that leverages the unique advantages of such environments to support the conception, assessment, and understanding of therapies for restoring upper limb functions in

rats. We anticipate that this platform will play a critical role for the development and understanding of new therapies that translate into treatments for humans.

MATERIALS AND METHODS

Study design

The overall study can be separated into three components: The first was a characterization of the neurorobotic platform to assess its functionality and capacity to quantify upper limb performance. The component was carried out on $n = 8$ rats. Because this was purely a descriptive experiment with no existing historical data, no power analysis was carried out to predetermine the group size.

The second was a rehabilitation study to compare robot-assisted upper limb rehabilitation with more conventional rehabilitation techniques. A group size $n = 5$ was selected for this experiment based on the results of a power calculation (G*Power) (*50*) using an effect size taken from our previous rehabilitation studies in the lower limb.

The third component was a case study performed to determine whether the characteristics of the neurorobotic platform could provide an advantageous environment for therapy development. In this case, a proof-of-concept experiment was carried out to assess whether targeted neuromodulation could ameliorate specific upper limb movements after SCI.

Design of the robotic interface

Here, we developed a robotic platform capable of providing differing levels of assistance during forelimb reaching movements in rats. Because the kinematic parameters of such reaching and grasping movements primarily involve a combination of three translational movements with a single rotatory component (*18*), the system has four DOFs: space translation and pronation/supination of the forelimb. The Cartesian workspace of the robot, calculated to overlap with the kinematics of the free forelimb movement (*51*), corresponds to an area of 56 mm by 40 mm by 20 mm for *x*, *y*, and *z* directions, respectively. Movement in the *yz* plane was achieved using a parallel kinematic chain, the design of which was based on the pantograph. Movement along the third axis (*x*) and rotatory component were realized using a linear slide (IKO BWU60-100, Nippon Thompson Co. Ltd.) and a customized parallel shift gear mechanism, respectively.

The pantograph structure was actuated by two brushed rotary DC motors (DCX 14 L, Maxon Motor, Switzerland), coupled with a gearbox (GPX 16 A 150:1, Maxon Motor, Switzerland) to reach 1.04 Nm of torque, with a high-resolution encoder (ENX 10 EASY, Maxon Motor, Switzerland) allowing precise measurements of the position of the actuator (fig. S1). Another rotary DC motor (DCX 08 L, Maxon Motor, Switzerland), coupled with a gearbox (GPX 8 A 216:1, Maxon Motor, Switzerland) and a magnetic encoder (ENX 8 MAG, Maxon Motor, Switzerland), controlled the pronation/supination movement (fig. S1). The linear slide was actuated by a brushless motor (EC-i 40, Maxon Motor, Switzerland) coupled with a spindle drive (GP 32 S, Maxon Motor, Switzerland). A Hall sensor and an encoder (ENC 16 EASY, Maxon Motor, Switzerland) allowed measurement of absolute position.

We aimed to design a versatile interface capable of guiding the rats' wrist along any trajectory within the entire workspace, both unassisted and fully assisted. For this purpose, we designed a soft magnetic clasp to gently yet securely clamp the wrist of the rat. After embracing the wrist, the clasp could be easily attached to the motion module of the R-Bot through magnets (QS-179173, Supermagnete, Switzerland), allowing a continuous monitoring of force and position of the forelimb (Fig. 1A).

A mobile restrainer module provides flexibility in the position of the animal, allowing it to be adapted to the position of the motion part of the R-Bot. To perform the task, rats were placed on the restrainer using a jacket over the torso of the animal and attached to a backplate using a Velcro strip (fig. S1). Depending on the needs of the specific experiment, animals could be fixed in a bipedal or quadrupedal position. Adjustment on the relative orientation and distance between the animal and the clasp position were obtained with two micrometric translational stages and two hinges. This module was switchable to choose the working paw according to the dexterity of the subject.

The robot device was sensorized with a six-axis load cell (Nano17, ATI Industrial Automation, USA), working with a sampling rate of 100 Hz. Moreover, two Hall effect position sensors (A1301, Allegro Microsystems) and a piezoelectric element were included in the robot to detect the extremities of the movement on the *x* axis and to signal to the animal the completion of each trial.

The real-time control of the R-Bot was conducted using CompactRIO 9030 (National Instruments Corp., Austin, TX). To perform coordinated high-performance multiaxis movements, the four motor drives (MAXPOS 50/5, Maxon Motor, Switzerland) were connected in series to the master real-time NI over EtherCAT (fig. S1).

The control of the system was realized with LabVIEW 2018 using Hybrid Mode that integrates the RIO Scan Interface and LabVIEW FPGA Module. In particular, analog input and output modules (NI 9220, NI, Austin, TX; NI 9263, NI, Austin, TX) were used in Scan Interface, while digital I/O module (NI 9401, NI, Austin, TX) ran in FPGA mode. A sequence structure divided the main code in three phases: starting, operating, and closing frames. In the operating phase, four tasks ran in parallel: The data acquisition used a timed-loop structure to implement tasks with high priority, and the other three tasks used while loops at different frequency rates. The first while loop regulated the movements of the four actuators. The second while loop (sampling rate, 10 Hz) was used to visualize the force signal and position of the motors in real time. The final while loop saved the acquired data from the FIFO memory buffer to the cRIO disk. Data were transferred offline from the memory of the CompactRIO to the computer through network communication.

A user-friendly graphical user interface (GUI) was designed to allow the setting of initial parameters and to visualize recorded data in real time. In particular, before starting, the task users could select options for a number of different variables: the number of repetitions of the movement, the specific task to be performed, which forelimb will be used (typically the animal's dominant forelimb), and the position of the animal (bipedal or quadrupedal). During the task, two panels allowed the visualization in real time of the down-sampled data recorded by the load cell and the position of the four actuators. In addition, a security button was included in the interface to immediately interrupt the movement of the robot at any moment of the cycle (Fig. 1B).

E-dura array fabrication

The soft spinal cord implant consisted of an electrode array connected by stretchable interconnects embedded in an ultrathin silicone matrix (80 μm), as previously described (*52*). Briefly, the electrical

tracks (200-μm width) were composed of a multilayer stack of silicon dioxide (SiO_2), polyimide (PI), titanium (Ti), and platinum (Pt) ordered in the following sequence: SiO_2 25 nm, PI 1 μm, Ti 20 nm, Pt 100 nm, Ti 20 nm, PI 1 μm, and SiO_2 25 nm. The thin films were patterned via photolithography and dry etching on a silicon wafer carrier to define the shape of the interconnects. The tracks feature a periodic micropattern that enabled their stretchability by allowing out-of-plane deflections under strain (*53*). A layer of polydimethylsiloxane (40 μm) was laser-cut and bonded on each side of the interconnects to form the soft silicone encapsulation, giving the device its final shape. The electrode contacts (140 μm by 500 μm) were coated with a soft platinum-silicone composite (*23*) via screen-printing to improve the charge injection properties and provide a soft interface with the tissue. The same conductive composite was used to establish electrical contact with a flexible printed circuit board on which a ground wire and a connector was soldered (Omnetics, A79042-001) for a transdermal connection on the head of the animal. This scheme was implemented in lieu of individual wires to provide a compact and robust interface with the external stimulator.

Animals and care

All experimental procedures were approved by the Veterinary Office of the Canton of Geneva, Switzerland and carried out in accordance with the National Institutes of Health *Guide for the Care and Use of Laboratory Animals*. Experiments were conducted on adult female Lewis rats (Janvier, France) housed in a 12-hour light/12-hour dark cycle in a specialized facility with controlled humidity and temperature. Animals were placed on a restricted diet to increase motivation to perform food reward–based functional tasks. Access to water was ad libitum.

Surgical procedures

All surgical procedures were carried out under gaseous anesthesia (1.5 to 2.5% isoflurane in medical oxygen).

Electromyographic implantation

Bipolar electromyographic (EMG) wires (Teflon-coated stainless steel wires; Cooner Wire) were implanted chronically into the spinodeltoideus, biceps brachii, triceps brachii, extensor carpi ulnaris, extensor carpi radialis, and/or extensor digitorum communis muscles and fixed in place with nondissolvable sutures. All electrodes were connected to a percutaneous head plug fixed to the skull using dental cement and bone screws.

E-dura array implantation

Connective tissue between C3/C4, C6/C7, and T1/T2 vertebrae was removed and a 4.0 Ethilon suture was fed under the cervical vertebrae, entering rostral of C4, and exiting caudal of T1. A loop was formed at the T1 end of Ethilon, and this was used to pull the e-dura array underneath the T1 vertebra, continuing until exiting the epidural space between C3 and C4. The array was then connected to a stimulus isolator (A-M Systems, USA), and the array position was optimized on the basis of observed muscle twitch responses to stimulation at each of the individual electrode sites. Bone screws were then inserted into T2 and T3 vertebrae, and the caudal end of the array was fixed in place between these screws using dental cement.

Hemicontusion injury

After baseline recordings, animals received a unilateral cervical SCI. A partial laminectomy was performed over the C5 spinal cord segment, and a controlled hemicontusion was delivered to the C5 spinal segment using an IH impactor (200 kdynes; Precision Systems and Instrumentation, USA). The injury was performed on the side of the dominant forelimb, as determined during training in the single-pellet reaching task.

Brain and spinal cord injections

Connective tissue between the C4/C5 and C5/C6 vertebrae was removed, and unilateral injections (on the side of the dominant forelimb) of 500 nl of rAAV2-hSyn-Cre (Addgene, #105553-AAVrg) were performed at each of the two exposed sites using a Nanoliter 2010 injection system [World Precision Instruments (WPI), USA] at a rate of 200 nl/min. At each of the two injection sites, a volume of 250 nl was injected at a depth of 1.7 mm, and 250 nl was injected at 0.7 mm. A craniotomy was then performed over the forelimb motor cortex, and injections of 250 nl of AAV5-CAG-Flex-GCaMP6m (Addgene, #100839-AAV5) or AAV5-CAG-Flex-TdTomato (viral vector core of Ecole Polytechnique Fédérale de Lausanne) were conducted using the same settings as for spinal injections and at the following coordinates (relative to bregma): +1 anterior/posterior (AP), ±2 medial/lateral (ML); +2 AP, ±2 ML; +1 AP, ±3 ML; +2 AP, ±3 ML. All injections were carried out at a depth of −1.5 mm from the surface of the brain and contralateral to the site of spinal injections.

Anatomical location of motor neurons

A skin incision was made over the relevant muscle (biceps brachii or triceps brachii), and a total of 5 to 6 μl of 8% FluoroRuby (Fluorochrome, USA) in sterile saline was injected over 8 to 10 separate injection sites in close proximity to the motor end plates of the relevant muscle using a 10-μl Hamilton syringe. The injection needle was left in place for 30 s after each injection to prevent backflow of tracer and nonspecific tracing.

Lens implantation for live calcium imaging

Animals receiving cortical injections of AAV5-Syn-Flex-GCaMP6m were also implanted with a ProView prism probe (1 mm diameter, 4.3 mm length; Inscopix, USA). After the cortical injections, a precise incision was made using a specialized microsurgical blade from +2 AP, ±2 ML to +2 AP, ±3 ML at a continual depth of −2.5 mm. The prism probe was then attached to the lens implant kit (Inscopix, USA), and the leading edge of the prism was slowly (50 μm/s) lowered directly into the incision site to a depth of −2 mm, with the flat face of the prism facing the injection sites. Metabond dental cement (C&B, Parkell, NY) and bone screws were used to securely fix the probe to the skull in this position. The top of the lens was then protected with a layer of Kwik-Cast (WPI, USA).

Four weeks after this implantation, a baseplate was attached to the lens cuff of the prism probe and adjusted before being fixed in place at the optimal position for detecting a clear image of $GCaMP^+$ neuronal cell bodies, with the nVista HD microscope attached (Inscopix, USA). After all surgical procedures, animals were provided with analgesia [buprenorphine (0.05 mg/kg) and carprofen (5 mg/kg), both delivered subcutaneously] and antibiotics (oral amoxicillin, 1 ml/100 ml drinking water for 7 days) when appropriate.

Forelimb tasks

Four different tasks were analyzed in the current study: robot fully assisted task, robot unassisted pulling task (retrieval), robot unassisted pushing task (reach), and the single-pellet reaching task (*23*). For each robot task, the animal was attached to the restrainer module, and its paw was blocked to the motion module of the robot through the clasp. In the fully assisted task, the whole movement was driven by the motors and the animal was completely passive. In the unassisted pulling task, the extension phase was executed by the motors, while the retraction of the paw (and consequently of the

motion module of the robot) was a voluntary action of the animal. Conversely, in the unassisted pushing task, the extension phase was executed by the animal and the retraction phase was a passive movement. During these last two tasks, the active phase of the trajectory was not determined a priori, and a single trial was considered accomplished when the rat's wrist reached the home or the target position in the *x* direction for the unassisted pulling task and the unassisted pushing task, respectively.

Multiple trajectories were implemented for both robot tasks: different linear trajectories to fill the whole working space, a trajectory limited to one DOF only, an elliptic movement on the *yz* plane, and a trajectory that reproduced the reaching movement. The single-pellet reaching task has been described in detail previously (*54*). Briefly, rats were trained to reach through a small window in a plexiglass cage and accurately grasp a single sugar pellet (sucrose, 45 mg; TestDiet, USA) placed on a platform outside the cage. This task is considered a gold standard in assessing rat forelimb performance and was thus used to evaluate the capability of the robot in assessing functionality before and after injury.

Kinematic, EMG, and neural recordings

The R-Bot was embedded in a system enabling recordings of forelimb kinematics, EMG activity, and neural signals. For kinematics, a motion capture system (SIMI Reality Motion Systems GmbH, Germany) was used to record video (50 Hz). Four high-quality cameras (1920 pixels by 1920 pixels) simultaneously recorded the area of interest. EMG signals were amplified and filtered (10- to 1000-Hz band-pass filtering) using a differential AC amplifier (A-M Systems, USA), recorded using PowerLab 8/35 (AD Instruments) with corresponding software (LabChart Pro v8, AD Instruments), and subsequently analyzed offline.

For calcium imaging of the forelimb motor cortex, nVista HD (Inscopix, CA) was used to acquire images at 20 Hz. A head-attached microscope with a resolution of 1440 pixels by 1080 pixels was securely attached to the baseplate at the beginning of every recording session to interface with the implanted lens. The imaging field of view was about 750 μm by 600 μm, and the depth of the focus plane was selected using the nVista software to observe clear Ca^{2+} signals in neuronal cell bodies.

EES protocols

Mapping of specificity

Once attached to the restrainer module, animals underwent a recruitment curve mapping protocol to identify which electrode was most specific for the biceps or triceps muscle. Briefly, while recording evoked EMG responses, 200-μs biphasic pulses of electrical stimulation at a frequency of 1 Hz were delivered at gradually increasing intensities of up to 500 μA. Stimulation was delivered using an isolated pulse stimulator (model 2100, A-M Systems, USA), and EMG responses were amplified, filtered, recorded, and visualized as previously described. During these sessions, experimenter observations were made of which muscles were recruited first and which muscles seemed to be responding most at each electrode position. Offline analysis was later conducted to calculate recruitment curves for each muscle, with data normalized to the maximal response evoked for each muscle using its optimal electrode on the array.

Continuous stimulation

Continuous stimulation was delivered from a user-defined electrode throughout task performance and 90% of the threshold to evoke detectable muscle twitches. Stimulation consisted of 200-μs biphasic pulses delivered in 10-ms bursts of 700 Hz every 20 ms. Stimulation was delivered using an isolated pulse stimulator (model 2100, A-M Systems, USA).

Activity-dependent stimulation

Stimulation frequency and intensity remained the same as those used for continuous stimulation. However, for this protocol, stimulation was only delivered while endogenous EMG activity for a user-selected muscle remained above a threshold set at 2× background noise. This real-time, closed-loop triggering of stimulation was controlled via an RZ2 processor (Tucker-Davis Technology, USA) that received live EMG signals, performed a root mean square to make all signals positive, applied the threshold to this signal, and then sent a signal to the stimulus isolator to deliver stimulation at all times when the EMG signal was above this threshold (Fig. 8C).

Statistical results

Variance analysis of the multivariate analysis of the group performing daily motor rehabilitation was performed with two-way repeated-measures analysis of variance (RM ANOVA), followed by a post hoc Tukey test, to evaluate variations in time and treatment. Variance analysis of the single-pellet reaching task and the multivariate analysis of the spontaneous group recovery were performed with one-way RM ANOVA, followed by a post hoc Tukey test, to evaluate variations in time. Comparison of the effects of epidural stimulation was carried out using a paired *t* test (two-tailed). For all the other statistical analysis, a nonparametric Kruskal-Wallis test was performed.

SUPPLEMENTARY MATERIALS

www.science.org/doi/10.1126/scirobotics.abk2378
Materials and Methods
Figs. S1 to S6
Table S1
Movie S1
References (*55*–*58*)

REFERENCES AND NOTES

1. K. D. Anderson, Targeting recovery: Priorities of the spinal cord-injured population. *J. Neurotrauma* **21**, 1371–1383 (2004).
2. L. A. Simpson, J. J. Eng, J. T. C. Hsieh, D. L. Wolfe; Spinal Cord Injury Rehabilitation Evidence Scire Research Team, The health and life priorities of individuals with spinal cord injury: A systematic review. *J. Neurotrauma* **29**, 1548–1555 (2012).
3. G. Courtine, M. V. Sofroniew, Spinal cord repair: Advances in biology and technology. *Nat. Med.* **25**, 898–908 (2019).
4. D. J. Reinkensmeyer, J. L. Patton, Can robots help the learning of skilled actions? *Exerc. Sport Sci. Rev.* **37**, 43–51 (2009).
5. S. Micera, M. Caleo, C. Chisari, F. C. Hummel, A. Pedrocchi, Advanced neurotechnologies for the restoration of motor function. *Neuron* **105**, 604–620 (2020).
6. W. S. Harwin, J. L. Patton, V. R. Edgerton, Challenges and opportunities for robot-mediated neurorehabilitation. *Proc. IEEE* **94**, 1717–1726 (2006).
7. R. van den Brand, J. Heutschi, Q. Barraud, J. DiGiovanna, K. Bartholdi, M. Huerlimann, L. Friedli, I. Vollenweider, E. M. Moraud, S. Duis, N. Dominici, S. Micera, P. Musienko, G. Courtine, Restoring voluntary control of locomotion after paralyzing spinal cord injury. *Science* **336**, 1182–1185 (2012).
8. H. I. Krebs, N. Hogan, M. L. Aisen, B. T. Volpe, Robot-aided neurorehabilitation. *IEEE Trans. Rehabil. Eng.* **6**, 75–87 (1998).
9. M. Coscia, M. J. Wessel, U. Chaudary, J. D. R. Millán, S. Micera, A. Guggisberg, P. Vuadens, J. Donoghue, N. Birbaumer, F. C. Hummel, Neurotechnology-aided interventions for upper limb motor rehabilitation in severe chronic stroke. *Brain J. Neurol.* **142**, 2182–2197 (2019).
10. L. Marchal-Crespo, D. J. Reinkensmeyer, Review of control strategies for robotic movement training after neurologic injury. *J. Neuroeng. Rehabil.* **6**, 20 (2009).
11. D. J. Reinkensmeyer, J. L. Emken, S. C. Cramer, Robotics, motor learning, and neurologic recovery. *Biomed. Eng.* **6**, 497–525 (2004).

12. C. Spalletti, S. Lai, M. Mainardi, A. Panarese, A. Ghionzoli, C. Alia, L. Gianfranceschi, C. Chisari, S. Micera, M. Caleo, A robotic system for quantitative assessment and poststroke training of forelimb retraction in mice. *Neurorehabilit. Neural Repair* **28**, 188–196 (2014).
13. M. Pasquini, S. Lai, C. Spalletti, M. Cracchiolo, S. Conti, A. Panarese, M. Caleo, S. Micera, A robotic system for adaptive training and function assessment of forelimb retraction in mice. *IEEE Trans. Neural Syst. Rehabil. Eng.* **26**, 1803–1812 (2018).
14. C. Spalletti, C. Alia, S. Lai, A. Panarese, S. Conti, S. Micera, M. Caleo, Combining robotic training and inactivation of the healthy hemisphere restores pre-stroke motor patterns in mice. *eLife* **6**, e28662 (2017).
15. A. L. A. Mascaro, E. Conti, S. Lai, A. P. D. Giovanna, C. Spalletti, C. Alia, A. Panarese, A. Scaglione, L. Sacconi, S. Micera, M. Caleo, F. S. Pavone, Combined rehabilitation promotes the recovery of structural and functional features of healthy neuronal networks after stroke. *Cell Rep.* **28**, 3474–3485.e6 (2019).
16. S. Conti, C. Spalletti, M. Pasquini, N. Giordano, N. Barsotti, M. Mainardi, S. Lai, A. Giorgi, M. Pasqualetti, S. Micera, M. Caleo, Combining robotics with enhanced serotonin-driven cortical plasticity improves post-stroke motor recovery. *Prog. Neurobiol.* **203**, 102073 (2021).
17. S. Navabpour, J. L. Kwapis, T. J. Jarome, A neuroscientist's guide to transgenic mice and other genetic tools. *Neurosci. Biobehav. Rev.* **108**, 732–748 (2019).
18. B. C. Vigaru, O. Lambercy, M. Schubring-Giese, J. A. Hosp, M. Schneider, C. Osei-Atiemo, A. Luft, R. Gassert, A robotic platform to assess, guide and perturb rat forelimb movements. *IEEE Trans. Neural Syst. Rehabil. Eng.* **21**, 796–805 (2013).
19. A. Erwin, C. Gallegos, Q. Cao, M. K. O'Malley, A robotic platform for 3D forelimb rehabilitation with rats. *IEEE Int. Conf. Rehabil. Robot.* **2019**, 429–434 (2019).
20. K. G. Sharp, J. E. Duarte, B. Gebrekristos, S. Perez, O. Steward, D. J. Reinkensmeyer, Robotic rehabilitator of the rodent upper extremity: A system and method for assessing and training forelimb force production after neurological injury. *J. Neurotrauma* **33**, 460–467 (2016).
21. S. A. Hays, N. Khodaparast, A. M. Sloan, T. Fayyaz, D. R. Hulsey, A. D. Ruiz, M. Pantoja, M. P. Kilgard, R. L. Rennaker, The bradykinesia assessment task: An automated method to measure forelimb speed in rodents. *J. Neurosci. Methods* **214**, 52–61 (2013).
22. N. Dominici, U. Keller, H. Vallery, L. Friedli, R. van den Brand, M. L. Starkey, P. Musienko, R. Riener, G. Courtine, Versatile robotic interface to evaluate, enable and train locomotion and balance after neuromotor disorders. *Nat. Med.* **18**, 1142–1147 (2012).
23. I. Q. Whishaw, S. M. Pellis, The structure of skilled forelimb reaching in the rat: A proximally driven movement with a single distal rotatory component. *Behav. Brain Res.* **41**, 49–59 (1990).
24. G. Courtine, J. Heutschi, R. van den Brand, Response to comment on "restoring voluntary control of locomotion after paralyzing spinal cord injury". *Science* **338**, 328 (2012).
25. S. G. Sotocina, R. E. Sorge, A. Zaloum, A. H. Tuttle, L. J. Martin, J. S. Wieskopf, J. C. Mapplebeck, P. Wei, S. Zhan, S. Zhang, J. J. McDougall, O. D. King, J. S. Mogil, The rat grimace scale: A partially automated method for quantifying pain in the laboratory rat via facial expressions. *Mol. Pain* **7**, 55 (2011).
26. A. J. Peters, J. Lee, N. G. Hedrick, K. O'Neil, T. Komiyama, Reorganization of corticospinal output during motor learning. *Nat. Neurosci.* **20**, 1133–1141 (2017).
27. M. D. Norenberg, J. Smith, A. Marcillo, The pathology of human spinal cord injury: Defining the problems. *J. Neurotrauma* **21**, 429–440 (2004).
28. F. F. Voigt, D. Kirschenbaum, E. Platonova, S. Pagès, R. A. A. Campbell, R. Kastli, M. Schaettin, L. Egolf, A. van der Bourg, P. Bethge, K. Haenraets, N. Frézel, T. Topilko, P. Perin, D. Hillier, S. Hildebrand, A. Schueth, A. Roebroeck, B. Roska, E. T. Stoeckli, R. Pizzala, N. Renier, H. U. Zeilhofer, T. Karayannis, U. Ziegler, L. Batti, A. Holtmaat, C. Lüscher, A. Aguzzi, F. Helmchen, The mesoSPIM initiative: Open-source light-sheet microscopes for imaging cleared tissue. *Nat. Methods* **16**, 1105–1108 (2019).
29. A. R. Ferguson, K.-A. Irvine, J. C. Gensel, J. L. Nielson, A. Lin, J. Ly, M. R. Segal, R. R. Ratan, J. C. Bresnahan, M. S. Beattie, Derivation of multivariate syndromic outcome metrics for consistent testing across multiple models of cervical spinal cord injury in rats. *PLOS ONE* **8**, e59712 (2013).
30. F. B. Wagner, J.-B. Mignardot, C. G. L. Goff-Mignardot, R. Demesmaeker, S. Komi, M. Capogrosso, A. Rowald, I. Seáñez, M. Caban, E. Pirondini, M. Vat, L. A. McCracken, R. Heimgartner, I. Fodor, A. Watrin, P. Seguin, E. Paoles, K. V. D. Keybus, G. Eberle, B. Schurch, E. Pralong, F. Becce, J. Prior, N. Buse, R. Buschman, E. Neufeld, N. Kuster, S. Carda, J. von Zitzewitz, V. Delattre, T. Denison, H. Lambert, K. Minassian, J. Bloch, G. Courtine, Targeted neurotechnology restores walking in humans with spinal cord injury. *Nature* **563**, 65–71 (2018).
31. E. M. Moraud, M. Capogrosso, E. Formento, N. Wenger, J. DiGiovanna, G. Courtine, S. Micera, Mechanisms underlying the neuromodulation of spinal circuits for correcting gait and balance deficits after spinal cord injury. *Neuron* **89**, 814–828 (2016).
32. N. Greiner, B. Barra, G. Schiavone, H. Lorach, N. James, S. Conti, M. Kaeser, F. Fallegger, S. Borgognon, S. Lacour, J. Bloch, G. Courtine, M. Capogrosso, Recruitment of upper-limb motoneurons with epidural electrical stimulation of the cervical spinal cord. *Nat. Commun.* **12**, 435 (2021).
33. N. Wenger, E. M. Moraud, J. Gandar, P. Musienko, M. Capogrosso, L. Baud, C. G. L. Goff, Q. Barraud, N. Pavlova, N. Dominici, I. R. Minev, L. Asboth, A. Hirsch, S. Duis, J. Kreider, A. Mortera, O. Haverbeck, S. Kraus, F. Schmitz, J. DiGiovanna, R. van den Brand, J. Bloch, P. Detemple, S. P. Lacour, E. Bézard, S. Micera, G. Courtine, Spatiotemporal neuromodulation therapies engaging muscle synergies improve motor control after spinal cord injury. *Nat. Med.* **22**, 138–145 (2016).
34. M. Capogrosso, T. Milekovic, D. Borton, F. Wagner, E. M. Moraud, J.-B. Mignardot, N. Buse, J. Gandar, Q. Barraud, D. Xing, E. Rey, S. Duis, Y. Jianzhong, W. K. D. Ko, Q. Li, P. Detemple, T. Denison, S. Micera, E. Bezard, J. Bloch, G. Courtine, A brain–spine interface alleviating gait deficits after spinal cord injury in primates. *Nature* **539**, 284–288 (2016).
35. I. R. Minev, P. Musienko, A. Hirsch, Q. Barraud, N. Wenger, E. M. Moraud, J. Gandar, M. Capogrosso, T. Milekovic, L. Asboth, R. F. Torres, N. Vachicouras, Q. Liu, N. Pavlova, S. Duis, A. Larmagnac, J. Voros, S. Micera, Z. Suo, G. Courtine, S. P. Lacour, Electronic dura mater for long-term multimodal neural interfaces. *Science* **347**, 159–163 (2015).
36. K.-A. Irvine, A. R. Ferguson, K. D. Mitchell, S. B. Beattie, A. Lin, E. D. Stuck, J. R. Huie, J. L. Nielson, J. F. Talbott, T. Inoue, M. S. Beattie, J. C. Bresnahan, The Irvine, Beatties, and Bresnahan (IBB) forelimb recovery scale: An assessment of reliability and validity. *Front. Neurol.* **5**, 116 (2014).
37. Z. Z. Khaing, S. A. Geissler, S. Jiang, B. D. Milman, S. V. Aguilar, C. E. Schmidt, T. Schallert, Assessing forelimb function after unilateral cervical spinal cord injury: Novel forelimb tasks predict lesion severity and recovery. *J. Neurotrauma* **29**, 488–498 (2012).
38. H.-N. Dai, L. MacArthur, M. McAtee, N. Hockenbury, J. L. Tidwell, B. McHugh, K. Mansfield, T. Finn, F. P. T. Hamers, B. S. Bregman, Activity based therapies to promote forelimb use after a cervical spinal cord injury. *J. Neurotrauma* **26**, 1719–1732 (2009).
39. D. Borton, S. Micera, J. D. R. Millán, G. Courtine, Personalized neuroprosthetics. *Sci. Transl. Med.* **5**, 210rv2 (2013).
40. V. R. Edgerton, G. Courtine, Y. P. Gerasimenko, I. Lavrov, R. M. Ichiyama, A. J. Fong, L. L. Cai, C. K. Otoshi, N. J. K. Tillakaratne, J. W. Burdick, R. R. Roy, Training locomotor networks. *Brain Res. Rev.* **57**, 241–254 (2008).
41. N. Estévez, N. Yu, M. Brügger, M. Villiger, M.-C. Hepp-Reymond, R. Riener, S. Kollias, A reliability study on brain activation during active and passive arm movements supported by an MRI-compatible robot. *Brain Topogr.* **27**, 731–746 (2014).
42. T. Mima, N. Sadato, S. Yazawa, T. Hanakawa, H. Fukuyama, Y. Yonekura, H. Shibasaki, Brain structures related to active and passive finger movements in man. *Brain* **122**, 1989–1997 (1999).
43. L. Asboth, L. Friedli, J. Beauparlant, C. Martinez-Gonzalez, S. Anil, E. Rey, L. Baud, G. Pidpruzhnykova, M. A. Anderson, P. Shkorbatova, L. Batti, S. Pagès, J. Kreider, B. L. Schneider, Q. Barraud, G. Courtine, Cortico–reticulo–spinal circuit reorganization enables functional recovery after severe spinal cord contusion. *Nat. Neurosci.* **21**, 576–588 (2018).
44. M. Bonizzato, G. Pidpruzhnykova, J. DiGiovanna, P. Shkorbatova, N. Pavlova, S. Micera, G. Courtine, Brain-controlled modulation of spinal circuits improves recovery from spinal cord injury. *Nat. Commun.* **9**, 3015 (2018).
45. M. Bonizzato, N. D. James, G. Pidpruzhnykova, N. Pavlova, P. Shkorbatova, L. Baud, C. Martinez-Gonzalez, J. W. Squair, J. DiGiovanna, Q. Barraud, S. Micera, G. Courtine, Multi-pronged neuromodulation intervention engages the residual motor circuitry to facilitate walking in a rat model of spinal cord injury. *Nat. Commun.* **12**, 1925 (2021).
46. N. Wenger, E. M. Moraud, S. Raspopovic, M. Bonizzato, J. DiGiovanna, P. Musienko, M. Morari, S. Micera, G. Courtine, Closed-loop neuromodulation of spinal sensorimotor circuits controls refined locomotion after complete spinal cord injury. *Sci. Transl. Med.* **6**, 255ra133 (2014).
47. J. von Zitzewitz, L. Asboth, N. Fumeaux, A. Hasse, L. Baud, H. Vallery, G. Courtine, A neurorobotic platform for locomotor prosthetic development in rats and mice. *J. Neural Eng.* **13**, 026007 (2016).
48. M. J. Wagner, J. Savall, T. H. Kim, M. J. Schnitzer, L. Luo, Skilled reaching tasks for head-fixed mice using a robotic manipulandum. *Nat. Protoc.* **15**, 1237–1254 (2020).
49. C. Pierella, E. Pirondini, N. Kinany, M. Coscia, C. Giang, J. Miehlbradt, C. Magnin, P. Nicolo, S. Dalise, G. Sgherri, C. Chisari, D. V. D. Ville, A. Guggisberg, S. Micera, A multimodal approach to capture post-stroke temporal dynamics of recovery. *J. Neural Eng.* **17**, 045002 (2020).
50. F. Faul, E. Erdfelder, A.-G. Lang, A. Buchner, G*Power 3: A flexible statistical power analysis program for the social, behavioral, and biomedical sciences. *Behav. Res. Methods* **39**, 175–191 (2007).
51. N. Vachicouras, O. Tarabichi, V. V. Kanumuri, C. M. Tringides, J. Macron, F. Fallegger, Y. Thenaisie, L. Epprecht, S. McInturff, A. A. Qureshi, V. Paggi, M. W. Kuklinski, M. C. Brown, D. J. Lee, S. P. Lacour, Microstructured thin-film electrode technology enables proof of concept of scalable, soft auditory brainstem implants. *Sci. Transl. Med.* **11**, eaax9487 (2019).
52. N. Vachicouras, C. M. Tringides, P. B. Campiche, S. P. Lacour, Engineering reversible elasticity in ductile and brittle thin films supported by a plastic foil. *Extreme Mech. Lett.* **15**, 63–69 (2017).

53. G. Schiavone, F. Fallegger, X. Kang, B. Barra, N. Vachicouras, E. Roussinova, I. Furfaro, S. Jiguet, I. Seáñez, S. Borgognon, A. Rowald, Q. Li, C. Qin, E. Bézard, J. Bloch, G. Courtine, M. Capogrosso, S. P. Lacour, Soft, implantable bioelectronic interfaces for translational research. *Adv. Mater.* **32**, 1906512 (2020).
54. K. Chung, K. Deisseroth, CLARITY for mapping the nervous system. *Nat. Methods* **10**, 508–513 (2013).
55. C. Pan, R. Cai, F. P. Quacquarelli, A. Ghasemigharagoz, A. Lourbopoulos, P. Matryba, N. Plesnila, M. Dichgans, F. Hellal, A. Ertürk, Shrinkage-mediated imaging of entire organs and organisms using uDISCO. *Nat. Methods* **13**, 859–867 (2016).
56. T. Nath, A. Mathis, A. C. Chen, A. Patel, M. Bethge, M. W. Mathis, Using DeepLabCut for 3D markerless pose estimation across species and behaviors. *Nat. Protoc.* **14**, 2152–2176 (2019).
57. E. S. Rosenzweig, G. Courtine, D. L. Jindrich, J. H. Brock, A. R. Ferguson, S. C. Strand, Y. S. Nout, R. R. Roy, D. M. Miller, M. S. Beattie, L. A. Havton, J. C. Bresnahan, V. R. Edgerton, M. H. Tuszynski, Extensive spontaneous plasticity of corticospinal projections after primate spinal cord injury. *Nat. Neurosci.* **13**, 1505–1510 (2010).
58. L. Sheintuch, A. Rubin, N. Brande-Eilat, N. Geva, N. Sadeh, O. Pinchasof, Y. Ziv, Tracking the same neurons across multiple days in Ca2+ imaging data. *Cell Rep.* **21**, 1102–1115 (2017).

Acknowledgments: We thank L. Baud, A. Bichat, and O. Rizzo for technical assistance with animal experiments; J. Ravier and M. Burri for assistance with figure design; G. Rizzi and L. Urban for support in neural recordings and analysis; and A. Melani for technical support. We also acknowledge the Advanced Lightsheet Imaging Center (ALICe) at the Wyss Center for Bio and Neuroengineering, Geneva for support in the light sheet imaging. **Funding:** This work was supported by the Friedrich Flick Förderungsstiftung through Wings for Life, Swiss National Science Foundation (NCCR Robotics, 310030_185214), European Research Council (ERC-2015-CoG HOW2WALKAGAIN 682999), the Bertarelli Foundation, and the Tuscany Government under the RONDA and PERSONA projects (Bando FAS Salute 2014 and 2018).
Author contributions: S.M., M.P., S.L., and J.C. conceived the characteristics of the R-Bot. M.P. designed and developed the R-Bot. S.M. supervised its design and development. S.A. performed the lens implantation surgeries, and N.D.J. performed all other surgeries. M.P., N.D.J., and I.D. collected and analyzed all the data. I.D., N.C., and Q.B. performed all the anatomical procedures. F.-V.C. and N.D.J. designed the e-dura array and F.-V.C. fabricated them. S.P.L. supervised the design and fabrication of the array. I.D., M.P., N.D.J., Q.B., and G.C. prepared the figures. G.C. wrote the manuscript with N.D.J., and all the other authors contributed to its editing. G.C. and S.M. supervised all aspects of the work. **Competing interests:** The authors declare competing financial interests: G.C., S.M., and S.P.L. hold various patents in relation with electrical spinal cord stimulation and are cofounders and shareholders of ONWARD Medical, a company that develops treatments for SCI with partial relationships with the presented work. **Data and materials availability:** All data needed to evaluate the conclusions in the paper are present in the paper or the Supplementary Materials. Source data are available at https://doi.org/10.5281/zenodo.6043459. All custom codes used for data analysis are available at the following GitHub repository: https://github.com/neurorestore/upperlimb_robot.

Submitted 14 July 2021
Accepted 3 March 2022
Published 30 March 2022
10.1126/scirobotics.abk2378

Science Robotics

Preclinical upper limb neurorobotic platform to assess, rehabilitate, and develop therapies

Maria Pasquini, Nicholas D. James, Inssia Dewany, Florent-Valéry Coen, Newton Cho, Stefano Lai, Selin Anil, Jacopo Carpaneto, Quentin Barraud, Stéphanie P. Lacour, Silvestro Micera, and Grégoire Courtine

Sci. Robot. **7** (64), eabk2378. DOI: 10.1126/scirobotics.abk2378

Science Robotics (ISSN 2470-9476) is published by the American Association for the Advancement of Science. 1200 New York Avenue NW, Washington, DC 20005. The title *Science Robotics* is a registered trademark of AAAS.